A Single-Cell Temporal Atlas of Mouse Nasal Embryonic Development

Huan Chen[a,b,1]; Yingxiu Chen[a,b,1]; Mengjie Pan[a,b,1]; Ziyu Feng[a,b,1]; Baomei Cai[a,b,1]; Yiyi Cheng[a,b]; Sihao Chen[a,b]; Jiehong Deng[a,b]; Xia Yao[a,b]; Chunhua Zhou[a,b]; Yunjing Du[a,b]; Wei He[a,b]; Ruifang Zhang[a,b]; Yudong Fu[a,b]; Shujuan Liu[a,c]; Lihui Lin[d]; Shengyong Yu[a]; Yuehong Yan[a,c]; Duanqing Pei[e]; Dajiang Qin[a,c]; Jiekai Chen[d]; Shangtao Cao[a,b]*

a. Guangzhou National Laboratory, The Fifth Affiliated Hospital of Guangzhou Medical University, Guangzhou 510005, Guangdong, China
b. Guangzhou National Laboratory, Guangzhou International Bio Island, Guangzhou 510005, Guangdong, China
c. Key Laboratory of Biological Targeting Diagnosis, Therapy and Rehabilitation of Guangdong Higher Education Institute, department of nephrology, The Fifth Affiliated Hospital of Guangzhou Medical University, Guangzhou, 510700, Guangdong, China
d. Guangzhou Institutes of Biomedicine and Health, Chinese Academy of Sciences, Guangzhou, 510530, Guangdong, China.
e. Laboratory of Cell Fate Control, School of Life Sciences, Westlake University, Hangzhou, 310030, Zhejiang, China

* Corresponding author. email: cao_shangtao@gzlab.ac.cn

[1]These authors contributed equally to this work.

Abstract

The mammals breathe and perceive odors through anatomically and functionally distinct respiratory and olfactory regions of the nose; however, how the early embryo endows this system remains largely unknown. Here, we present a temporal high-resolution single-cell RNA sequencing (scRNA-seq) atlas of mouse nasal development, comprising 183,247 cells collected from 20 embryos spanning embryonic day 10.5 (E10.5) to E18.5. We identified 7 major cell clusters and 52 molecularly defined subtypes, including previously unrecognized rare populations and niche-derived signaling components involved in progenitor cell maintenance. Lineage reconstruction of epithelial and mesenchymal compartments revealed dynamic cell fate transitions and highlighted candidate regulators of lineage specification, including *Foxa1* as a regulator of nasal respiratory ciliated epithelium differentiation. Integration with adult nasal epithelium datasets further delineated transcriptional dynamics of olfactory stem cells. This study provides a molecular roadmap of nasal development and offers a valuable resource for future research into nasal biology and regenerative strategies.

Keywords

Nasal development, temporal atlas, progenitor cell maintenance, lineage trajectories, *Foxa1*

Introduction

The nose is a principal respiratory and sensory organ in vertebrates, primarily responsible for air filtration, olfaction, and immune defense. Over the past decades, significant progress has been made in understanding nasal development from anatomical and histological perspectives (Cuschieri and Bannister, 1975; Kim et al., 2004; Sokpor et al., 2018; Kim et al., 2023; Parslow et al., 2024). More recently, single-cell technologies have enabled the construction of cellular atlases of the adult nasal epithelium or individual developmental stage, with most studies focusing on the olfactory region (Tsukahara et al., 2021; Horgue et al., 2022; Amato et al., 2024; Hills et al., 2024; Ualiyeva et al., 2024; Yang et al., 2024; Taroc et al., 2025). However, the

molecular and cellular mechanisms underlying embryonic nasal development remain largely unclear, particularly how diverse cell populations coordinate to shape nasal structures during early development.

Embryonic nasal development is a complex and tightly regulated process. In mice, as in most mammals, the nasal placode arises from the frontonasal process and undergoes sequential morphogenesis through intricate epithelial–mesenchymal interactions (LaMantia et al., 2000; Streit, 2004; Balmer and LaMantia, 2005; Chen et al., 2009; Maier et al., 2011; Forni et al., 2013; Cho et al., 2019). The surface ectoderm thickens and invaginates into the underlying mesenchyme, forming the nasal pit by embryonic day 10.5 (E10.5), which gives rise to the primitive respiratory and olfactory epithelium and forms cavities through repeated tissue folding. Concurrently, mesoderm and neural crest–derived mesenchymal cells differentiate to shape the nasal framework via chondrogenesis and osteogenesis (Katoh et al., 2011; Suzuki and Osumi, 2015). These events are orchestrated by multiple conserved signaling pathways, including FGF, BMP, WNT, SHH and TGF-β, which regulate regional patterning and cell fate specification (Gong et al., 2009; Gokoffski, 2010; Maier et al., 2010; Maier et al., 2011; Forni et al., 2013; Zhu et al., 2016). Despite these well-characterized morphogenetic events, the detailed cellular composition, dynamic changes, and molecular regulation during the embryonic stages remain incompletely understood. In particular, the identification and characterization of nasal stem and progenitor cells, as well as the regulatory mechanisms guiding their lineage commitment, especially toward the respiratory epithelium, are still poorly defined.

To address these gaps, we generated a high-resolution single-cell RNA sequencing (scRNA-seq) temporal atlas of mouse nasal development during embryogenesis. This dataset allowed us to uncover previously unrecognized cell subtypes, novel marker genes, and niche-derived factors involved in progenitor cell maintenance. By reconstructing lineage trajectories of both epithelial and mesenchymal compartments, we identified key regulators governing cell fate decisions, notably highlighting the role of *Foxa1* in specifying

the ciliated lineage of nasal respiratory epithelium. Furthermore, by integrating our dataset with published adult nasal epithelium atlases, we systematically traced the transcriptional dynamics of globose basal cells within the olfactory epithelium. Together, our study provides a molecular and cellular roadmap of mouse nasal development at single-cell resolution. It not only advances fundamental knowledge of nasal morphogenesis but also establishes a valuable resource for future studies on gene regulation, congenital nasal disorders, and regenerative medicine.

Results

scRNA-seq atlas of mouse nasal embryonic development

To systematically characterize the cellular composition and transcriptional dynamics underlying nasal morphogenesis at single-cell resolution, we collected mouse embryos from embryonic day 10.5 (E10.5) to E18.5 at 24-h intervals, and performed precise microdissection of nasal tissues, with at least two biological replicates for each stage (Figs. 1A and S1A). Single-cell suspensions were processed using the 10x Genomics platform, and after quality control, we obtained a developmental dataset comprising 183,247 high-quality cells, with a median of 3,777 detected genes and 12,822 UMIs per cell (Fig. S1B and S1C; Table S1). Uniform Manifold Approximation and Projection (UMAP) revealed a continuous trajectory of cellular states that recapitulated developmental progression (Fig. S1D). Pseudo–bulk principal component analysis (PCA) further demonstrated a robust temporal ordering along the first principal component (PC1), closely aligned with the actual developmental timeline, supporting the robustness and reproducibility of the dataset (Fig. S1E).

Utilizing this dataset, we first annotated and identified seven major cell populations (Fig. 1B and 1C). These included: non-neurogenic epithelium (*Epcam*$^{+}$/*Cdh1*$^{+}$/*Krt14*$^{+}$) and neurogenic epithelium (*Sox2*$^{+}$/*Pax6*$^{+}$/*Tubb3*$^{+}$) (Roskams et al., 1998; Amato et al., 2024; Taroc et al., 2025) which collectively expanded from 25.4% to 51.2% during development and formed the functional mucosal compartments of the nasal cavity (Figs. 1D, 1E, S1F). Mesenchymal

cells (*Twist1*$^{+}$/*Col1a2*$^{+}$/*Pdgfra*$^{+}$), constituted predominant population, decreasing from 58.3% to 40.2%, consistent with progressive epithelialization and structural remodeling (Fig. 1D and 1E). We also identified glial cells (*Sox10*$^{+}$/*Fabp7*$^{+}$/*Mpz*$^{+}$), derived from neural crest lineages (Barraud et al., 2010; Forni et al., 2011; Katoh et al., 2011; Perera et al., 2020; Senf et al., 2025; Taroc et al., 2025), endothelial cells (*Pecam1*$^{+}$/*Cdh5*$^{+}$/*Kdr*$^{+}$) that establish vascular networks, immune populations (*Cd48*$^{+}$/*Itgb2*$^{+}$/*Ptprc*$^{+}$) and erythrocytes (*Hba-a1*$^{+}$/*Hba-a2*$^{+}$/*Hbb-bs*$^{+}$), supporting metabolic supply (Fig. 1B–1D).

To further dissect the cellular heterogeneity within these major classes, we performed iterative sub-clustering and identified 52 molecularly distinct subtypes spanning progenitor, intermediate, and differentiated states across epithelial and mesenchymal lineages (Fig. 1F; Table S2). This analysis uncovered a spectrum of lineage-specific populations that emerged in a stage-dependent manner, providing a detailed view of nasal cellular diversification (Figs. 1F and S2A).

To delineate transcriptional dynamics related to developmental chronology, we performed correlation analysis of single-cell transcriptomes across all populations along the temporal continuum. The results revealed four transcriptionally distinct stages (Fig. S2B and S2C). Stage 1 (E10.5–E11.5) was characterized by enrichment of cell cycle regulation, telomere organization, and stem cell population maintenance, indicative of rapid proliferative expansion. Stage 2 (E12.5–E13.5) featured gene programs associated with stem cell differentiation and epithelial morphogenesis, reflecting establishment of region-specific lineages. Stage 3 (E14.5–E15.5) showed progressive upregulation of extracellular matrix organization and cartilage development genes, consistent with formation of nasal structural frameworks (Kaucka et al., 2018). Stage 4 (E16.5–E18.5) was enriched with ATP metabolic process and metal ion and oxidative stress response, suggesting functional maturation of nasal tissue (Fig. S2B and S2C).

Collectively, we generated a high-resolution, temporally resolved mouse nasal

embryonic development cell atlas (mNEDCA). This resource enables us to further identify more novel molecular and cellular features and investigate how different cell populations coordinate embryonic nasal development.

Molecular characterization of the embryonic nasal epithelium

The nasal epithelium constitutes the primary interface for respiration and olfaction and also contributes to neuroendocrine and reproductive functions (Chung et al., 2016). It comprises multiple regionally specialized domains, including the respiratory epithelium (RE), olfactory epithelium (OE), vomeronasal organ (VNO), squamous epithelium (SE), septal organ (Ma et al., 2003; Tian and Ma, 2008), Grueneberg ganglion (Fuss et al., 2005), and migratory neuronal populations such as GnRH-1 and terminal neurons (Parslow et al., 2024). Despite this anatomical complexity, transcriptional profiles and reliable markers for these region-specific epithelial cell types during embryogenesis remain incompletely defined at single-cell resolution.

To delineate epithelial diversity, we performed in-depth analysis of the neurogenic and non-neurogenic epithelial compartments within mNEDCA, comprising 65,360 cells. Unbiased clustering resolved seven epithelial lineages corresponding to RE, OE, VNO, SE, GnRH-1 neurons, terminal neurons and a neural crest-like epithelial population (Fig. 2A and 2B). All clusters expressed canonical nasal epithelial markers (*Epcam/Six3*) (Rodenburg et al., 2023), whereas each lineage displayed distinct regional signatures (Fig. 2C; Table S3). The RE was characterized by *Foxa1* (Besnard et al., 2004; Wan et al., 2005; Paranjapye et al., 2020; Kusumoto et al., 2025; Taroc et al., 2025) and maintained a relatively stable proportion across stages (Figs. S3A, S3C, 2E). We identified previously underappreciated RE-enriched genes including *Serpinb11*, *Reg3g* and *Lox* (Fig. 2C), and functional enrichment with pathways involved morphogenesis of a branching epithelium and WNT signaling (Fig. S3B).

194 The OE represented the largest epithelial population (Fig. 2D) and was defined
195 by established markers *Omp* (Buiakova et al., 1996), *Foxg1* (Duggan et al.,
196 2008), and *Neurog1* (Shaker et al., 2012). Beyond these classic signatures, our
197 analysis highlighted *Cyp4v3*, *Cldn9* and *Rprm* as regional markers of OE (Fig.
198 2D). OE-enriched genes were associated with axonogenesis and synapse
199 assembly (Fig. S3B). smFISH confirmed OE-specific expression of *Cyp4v3* (Fig.
200 2F), a member of the cytochrome P450 family, which participated in lipid
201 metabolism and steroid hormone biosynthesis (Jia et al., 2023). *Cldn9*,
202 encoding a tight junction protein, may contribute to olfactory epithelium barrier
203 integrity (Nakano et al., 2009; Bird et al., 2010).
204
205 Apart from RE and OE, the rodent-specific structure vomeronasal organ (VNO)
206 was well distinguished by typical markers *Fezf2*/*Car2* (Eckler et al., 2011) and
207 novel specific genes like *Dlx6os1* and *Dync1i1*. VNO associated genes were
208 enriched in cellular response to monoamine stimulus and hormone secretion
209 (Fig. S3B). Squamous epithelium (SE) in the nasal vestibule expressed
210 canonical keratinocyte markers *Krtdap*/*Tfap2b* (Van Otterloo et al., 2022) and
211 was characterized by enrichment of skin development and keratinocyte
212 differentiation (Fig. S3B). We also identified *Gnrh1*$^{+}$/*Axo2*$^{+}$ GnRH-1 neurons
213 and *Prokr2*$^{+}$/*Prph*$^{+}$ terminal neurons (Figs. 2C and S3A) (Duittoz et al., 2022;
214 Amato et al., 2024). Unlike other epithelial clusters above appearing at E10.5,
215 the neural crest-derived epithelial subset emerged at E13.5 and specifically
216 express *Sox10*/*Foxc1* as well as novel genes like *Irx1*/*Cited4*, showing robust
217 enrichment in neural crest cell development, differentiation and migration (Figs.
218 2C and S3B).
219
220 Among these major epithelial lineages, embryonic RE heterogeneity has been
221 poorly characterized. Sub-clustering resolved ten RE populations with distinct
222 molecular identities (Fig. S4A and S4B). Progenitors were marked by
223 *Fgf8*/*Dlk1*/*Bmp4* (Kawauchi et al., 2005; Maier et al., 2010; Kitagaki et al., 2011;

224 Maier et al., 2011; Forni et al., 2013), whereas the basal compartment
225 (*Trp63*$^{+}$/*Dlk2*$^{+}$) comprised a proliferative *Top2a*$^{+}$ subset (Fig. S4B) (Deprez et
226 al., 2020) and two differentiating branches defined by *Irx3*$^{+}$/*Smoc2*$^{+}$ and
227 *Wnt10a*$^{+}$/*Serpinb2*$^{+}$ (Fig. S4B). Secretory lineages (*Cyp2f2*$^{+}$/*Serpinb11*$^{+}$)
228 segregated into proliferative secretory cells, mature secretory cells,
229 *Gp2*$^{+}$*Wfdc18*$^{+}$ goblet cells, and *Muc5b*$^{+}$*Tff2*$^{+}$ glandular mucous cells (Fig. S4B)
230 (Ualiyeva et al., 2024). Strikingly, within the ciliated population
231 (*Foxj1*$^{+}$/*Deup1*$^{+}$/*Myb*$^{+}$) (Yu et al., 2008), we identified a previously unrecognized
232 subcluster specifically expressing *Sftpc* (Fig. 2G and 2H), a canonical alveolar
233 type II marker (Treutlein et al., 2014). smFISH and immunofluorescence
234 confirmed co-localization of *Sftpc* with *Foxj1* and acetylated tubulin (Figs. 2I
235 and S4C). *Sftpc*$^{+}$ ciliated cells were enriched for genes involved in microtubule-
236 based motility and cilium movement, whereas *Sftpc*$^{-}$ ciliated cells preferentially
237 expressed cell-cycle and ciliogenesis regulators (*Cdkn1a*, *Stmn1*, *Ccno*) (Fig.
238 S4D and S4E; Table S4). These findings suggest functional diversification
239 within RE ciliated cells and implicate the *Sftpc*$^{+}$ subset in surfactant-related
240 regulation of nasal mucosal homeostasis.
241
242 We next dissected OE heterogeneity and annotated 12 populations (Fig. S5A–
243 S5C). Stem and progenitor compartments included *Sox2*$^{+}$/*Pax6*$^{+}$/*Rprm*$^{+}$
244 olfactory progenitors (Krolewski et al., 2012), *Sox2*$^{+}$/*Ascl1*$^{+}$/*Kit*$^{+}$ globose basal
245 cells (Paronett et al., 2023), and *Trp63*$^{+}$/*Krt14*$^{+}$/*Nrcam*$^{+}$ horizontal basal cells
246 (Kawauchi et al., 2004; Packard et al., 2011). Neurogenic lineages comprised
247 proliferative *Neurod1*$^{+}$/*Mki67*$^{+}$ immediate neuronal precursors (INPs),
248 *Neurog1*$^{+}$ INPs, *Ncam1*$^{+}$ immature olfactory sensory neurons (OSNs), and
249 Omp^{+} mature OSNs (Fig. S5B) (Graziadei et al., 1980; Cau et al., 2002;
250 McIntyre et al., 2010; Ualiyeva et al., 2024). Remarkably, INPs and immature
251 OSNs were detectable as early as E10.5, coinciding with the emergence of
252 migratory GnRH-1 and terminal neurons (Figs. S5C and 2E), consistent with
253 rapid initiation of olfactory neurogenesis following pit formation (Cau et al., 2002;

Taroc et al., 2020). Non-neurogenic lineages included sustentacular trajectories from proliferative *Cyp2g1*$^{+}$/*Mki67*$^{+}$ progenitors (Gu et al., 1999) to mature *Ermn*$^{+}$/*Cpm*$^{+}$ and *Cyp2g1*$^{+}$/*Pon1*$^{+}$ states, as well as *Ascl3*$^{+}$/*Foxi1*$^{+}$ microvillar and *Bpifb5*$^{+}$/*Kcnn4*$^{+}$ serous cells (Fig. S5B) (Ualiyeva et al., 2024). Comparable subtype diversity was also resolved in VNO (Katreddi and Forni, 2021; Katreddi et al., 2022; Lin et al., 2022; Hills et al., 2024; Dietz et al., 2025), SE (Yu et al., 2020; Ye et al., 2022), and neural crest–derived compartments (Fig. S6A–S6F).

Together, these analyses define the molecular landscape of embryonic nasal epithelial lineages and reveal regional and intra-lineage heterogeneity. In particular, the discovery of a *Sftpc*$^{+}$ ciliated population highlights previously unappreciated functional diversity within the respiratory epithelium and provides new entry points for investigating nasal epithelial specialization.

Heterogeneity of the embryonic nasal mesenchyme

In addition to the nasal epithelium, the nasal mesenchyme plays an indispensable role in nose development. Mesenchyme-derived cavity structures define nasal shape and, together with the soft palate and mouth, contribute to voice production (LaMantia et al., 2000; Yang et al., 2018). In our mNEDCA dataset, nasal mesenchyme represented the largest population among seven major cell clusters, underscoring its essential function in providing the structural matrix for nasal morphogenesis. However, the precise cellular composition and dynamic changes of this compartment during embryonic development remain poorly understood.

To this end, we performed an in-depth analysis of 105,140 mesenchymal cells, classifying them into ten transcriptionally distinct subpopulations using established marker genes (Fig. 3A–3C). Among them, two progenitor populations were identified: mesenchymal stem cells (MSCs) and mesenchymal progenitor cells (MPCs). Both exhibited high expression of stemness markers *Pax7*/*Hmga2* (Murdoch et al., 2010) and proliferation-

associated genes (*Top2a*, *Mki67*) but showed minimal expression of lineage-specific differentiation markers (Fig. 3C). Temporally, MSCs predominated at early developmental stages but disappeared after E12.5, whereas MPCs emerged at E11.5 and persisted until E18.5 (Fig. 3D and 3E). While MSCs and MPCs shared numerous cell cycle and stemness related genes, they displayed distinct transcriptional programs. MSCs were enriched for genes regulating serine/threonine kinase activity and stem cell maintenance, whereas MPCs expressed genes involved in extracellular matrix organization, connective tissue development, and cell fate specification (Fig. 3F and 3G). These observations suggest MPCs serve as a fate-committed intermediate between MSCs and differentiated mesenchymal lineages.

The remaining eight mesenchymal subtypes were classified into four main differentiation lineages: chondrogenic, osteogenic, fibroblastic, and pericytic. Chondrocytes (*Matn1*$^{+}$/*Acan*$^{+}$) (Hojo and Ohba, 2019) secreted type II collagen and proteoglycans, while osteoblasts (*Aspn*$^{+}$/*Ogn*$^{+}$/*Runx2*$^{+}$) (Fujita et al., 2004) formed nasal bones and cribriform plates, providing mechanical support. Pericytes (*Rgs5*$^{+}$/*Acta2*$^{+}$) (Berger et al., 2005) contributed to microvascular stability, and fibroblasts mediated connective tissue morphogenesis and basement membrane scaffolding (Figs. 3C and S7A; Table S5). Consistent with the stage 3 developmental features above (Fig. S3C and S3D), these differentiated cell types expanded markedly after E13.5 (Fig. 3E), indicating their crucial role in establishing nasal architecture.

Next, to verify MPCs as potential fate-committed intermediate, we employed RNA velocity and partition-based graph abstraction (PAGA) analysis (Wolf et al., 2019) to reconstruct lineage trajectories of nasal mesenchyme. As expected, the result revealed that MSCs transition through MPCs before differentiating into multiple mesenchymal lineages (Fig. S7B–S7D). Following this developmental trajectory, we performed single-cell regulatory network inference (SCENIC) analysis (Aibar et al., 2017) to investigate key transcription factors (TFs) governing nasal mesenchymal cell fate transition. Consistent with previous reports, the identification of known TFs like *Hmga2* and *Alx3* (Fig. 3H

and 3I) (Beverdam and Meijlink, 2001; Negishi et al., 2022) which highly expressed and activated in MSCs validate the analytical approach. Furthermore, we showed novel TFs regulators such as *Foxp1*/*Etv4* in MSCs and *Nfix*/*Junb* in MPCs, implying their regulatory roles in fate determination (Fig. 3H and 3I).

On the other hand, the subsequent differentiation programs were orchestrated by distinct lineage-determining transcriptional regulators. For instance, *Sox9* and *Plagl1* governed chondrogenesis (Akiyama, 2008), regulating both early commitment and terminal maturation. *Maf* and *Klf13* emerged as regulator directing fibroblast lineage specification (Fig. S7E and S7F). The osteogenic lineage was controlled by a *Dlx5* that progressively upregulated bone matrix genes (Samee et al., 2008), while *Ets1* and *Mef2c* regulated pericyte differentiation (Fig. S7E and S7F). Several additional TF candidates were identified that may represent novel regulators requiring further investigation.

Collectively, our results revealed the transcriptional diversity of nasal mesenchyme and support a model in which MPCs function as fate-committed intermediates guiding mesenchymal cell lineage differentiation during nasal morphogenesis.

Diverse signals governing RE progenitor cells maintenance

The rich diversity and distinct origins of cells participating in embryonic nasal development imply intricate intercellular communication underlying nasal morphogenesis. To elucidate these interactions, we conducted systematic ligand–receptor analyses across major cell types in mouse nasal development. Quantitative mapping of outgoing and incoming signals identified the nasal non-/neurogenic epithelium, mesenchyme, and glial cells as predominant communicators (Fig. 4A and 4B), with mesenchymal (e.g., *Bmp4*, *Wnt5a*) and glia-derived signals (e.g., *Wnt6*, *Dhh*, *Bmp7*) collectively accounting for ~50% of epithelial inputs, highlighting the established roles of BMP, WNT, and NOTCH pathways in nasal development (LaMantia et al., 2000; Sokpor et al., 2018). The segregation of olfactory and respiratory epithelium is directed by

351 antagonistic FGF and BMP signaling (Maier et al., 2010). In both chick and
352 mouse models, elevated BMP activity, marked by pSmad1/5/8 and activation
353 of *Msx1/2* and *Id3*, promotes respiratory epithelial fate, whereas BMP
354 antagonists, including *Noggin*, are required to preserve the neurogenic sensory
355 domain (Forni et al., 2013). In addition, autocrine signals from the epithelium
356 (*Fgf9*, *Nrg1*, *Ocln*) also contributed to self-regulation (Fig. S8A). These results
357 suggested that paracrine and autocrine signals cooperatively modulated global
358 nasal epithelial development.
359
360 Focusing on epithelial subtypes, we found that OE development was primarily
361 driven by mesenchymal inputs (32.5%), with WNT pathways critically regulating
362 sensory cell fate and morphogenesis, which resembled global epithelial cells
363 communication pattern (Kawauchi et al., 2004) (Fig. S8B and S8C). However,
364 RE development relied more heavily on autocrine signaling (34.0%) than that
365 from mesenchyme, glia or other cell types (Fig. S8D and S8E). This suggested
366 that RE development might involve special signaling patterns, which inspired
367 us to conduct further analysis of RE subclusters.
368
369 Then, we performed ligand-receptor interaction analysis for respiratory
370 epithelial progenitor cells (RE pro.), whose microenvironments for self-renewal
371 and differentiation were previously underestimated due to unavailable in vitro
372 culture models. The results revealed that autocrine signaling accounted for the
373 highest proportion with 39.4% (Fig. 4C). Specifically, it involves autocrine
374 signaling pathway including NOTCH (*Dlk1-Notch2/3*), FGF (*Fgf8*/*Fgf10-Fgfr2*
375 and *Fgf9-Fgfr1*) and WNT (*Wnt5a-Fzd3*) as well as ECM signaling (*Col9a1-*
376 *Sdc4*) (Fig. 4D; Table S6). Furthermore, we observed that ligands *Dlk1*, *Fgf8*,
377 *Fgf10* and *Wnt5a* highly expressed in RE pro. during early development, but
378 declined at later stages (Fig. 4E and 4F), suggesting a role in progenitor
379 homeostasis.
380
381 To test this, we decided to utilize these signals agonist, inhibitor and their
382 combinations to establish an in vitro culture system of RE progenitor cells
383 isolated from E11.5 nasal epithelial tissues. Ultimately, we developed one

384 chemically defined medium ("All" medium) to capture RE progenitors in vitro,
385 which consisted of three core small molecules FGF8, DAPT (NOTCH inhibitor)
386 and HRX215 (WNT/NOTCH modulator) (Zwirner et al., 2024) alongside
387 supplementary factors. Under these conditions, RE progenitor cells maintained
388 compact and smooth spheroid morphology (Fig. 4G), and sustained the
389 expression of progenitor markers *Fgf8*, *Dlk1*, *Wnt5a* and *Hmga2* by both qPCR
390 and bulk RNA-seq (Fig. 4H and 4I). On the contrary, removal of the three core
391 factors ("All-3C" medium) induced cystic structures from compact morphology
392 rapidly (Fig. 4G). Furthermore, we observed that differentiated genes such as
393 *Aqp5*, *Cyp2g1* and *Scgb1c1* upregulated obviously in the absence of these
394 three core small molecules (Fig. 4I). GO term analysis showed upregulated
395 genes were enriched in epithelial cell migration and regulation of metal ion
396 transport while decreased genes were related to DNA replication, rRNA
397 metabolic process and cell cycle regulation (Fig. 4J). These results confirmed
398 that the FGF, WNT and NOTCH signaling played important roles in establishing
399 essential microenvironments for RE progenitor cell maintenance in vitro (Fig.
400 4K).
401
402 Together, these analyses reveal a previously unappreciated autocrine-
403 dominant niche governing RE progenitors and provide evidence that
404 FGF/NOTCH/WNT mediated circuits sustain progenitor identity. The culture
405 system established here offers a platform for mechanistic dissection of
406 respiratory epithelial lineage specification.
407
408 **Foxa1 as a key regulator of respiratory epithelium differentiation**
409 The in vitro culture system for RE progenitor cells described above enabled
410 further investigation of key regulators of RE lineage differentiation predicted by
411 the mNEDCA dataset. Among these, transcription factors (TFs) represent major
412 drivers of cell fate transitions during development. To elucidate the roles of TFs
413 in RE development, we first performed trajectory analysis using RNA velocity
414 (Figs. 5A and S9A), which revealed that RE progenitor cells serve as the
415 developmental origin, giving rise to proliferative basal stem cells. These basal

stem cells subsequently diverged into two distinct lineages: a basal cell lineage generating *Irx3*$^{+}$ and *Wnt10a*$^{+}$ basal cell subtypes, and a secretory–ciliated lineage in which secretory progenitors either differentiated into secretory cells or *Gp2*$^{+}$*Wfdc18*$^{+}$ goblet cells or underwent terminal differentiation into *Foxj1*$^{+}$*Myb*$^{+}$ ciliated cells (Fig. 5A–5C, S9B). This bifurcating differentiation program was consistently supported by trajectory inference analyses with Monocle2 (Qiu et al., 2017) (Fig. S9C).

To identify TFs initiating RE differentiation, we performed comparative transcriptomic analysis between RE progenitor cells and their differentiated counterparts (RE differentiated cells) (Fig. S9D). RE progenitor cells exhibited high expression of stemness-associated genes (*Fgf8*) and TFs such as *Hmga2*, *Pax3*, and *Sp5*. In contrast, differentiated cells showed progressive upregulation of maturation markers (*Reg3g*, *Cyp2f2*, *Anxa5*) as well as TFs including *Foxa1*, *Cebpd*, and *Junb* along pseudotemporal ordering (Figs. 5D and S9E; Table S7). SCENIC analysis of TF–gene regulon activity further identified *Hmga2* and *Sp5* as key regulators maintaining RE progenitor cell identity, while *Foxa1* and *Cebpd* emerged as central drivers orchestrating RE lineage differentiation (Fig. 5E). Notably, SCENIC predicted *Deup1*, *Kcne3*, *Atp10d*, *Wdr19*, and *Aqp4* as downstream targets of *Foxa1*, all of which are activated during differentiation and participate in cilium assembly and motility pathways (Figs. 5F and S9F). Consistent with these predictions, smFISH confirmed restricted *Foxa1* expression within the RE region (Fig. S3C).

To functionally validate *Foxa1*, we overexpressed Foxa1 in RE progenitor cells via retroviral transduction (Figs. 5G and S9G), which significantly upregulated ciliogenesis-related genes including *Foxj1*, *Dynlrb2*, *Aqp4*, and *Ccno* as revealed by RNA-seq (Fig. 5H). Gene ontology (GO) analysis indicated enrichment for pathways related to cilium movement and glutathione metabolism (Fig. 5I), which was further confirmed by RT–qPCR validation (Fig. 5J).

Together, these findings delineated the differentiation trajectory of the

449 respiratory epithelium and demonstrated that *Foxa1* functions as a key
450 regulator of RE differentiation, directing progenitor cells toward the ciliated cell
451 lineage.
452
453 **Olfactory epithelial stem cell dynamics**
454 Compared with respiratory epithelial progenitor cells, olfactory epithelial (OE)
455 stem cells have attracted greater attention, yet the precise identity of stem cell
456 populations within the OE remains under debate. Globose basal cells (GBCs)
457 have been proposed as one candidate, given their molecular features and
458 phenotypic similarity to olfactory placode progenitor cells (OPPs), which
459 generate the OE during embryogenesis (Kawauchi et al., 2004; Packard et al.,
460 2011; Krolewski et al., 2012). However, accumulating evidence indicates that
461 GBCs constitute a heterogeneous population (Krolewski et al., 2013; Schwob,
462 J. E. et al., 2017). This apparent paradox prompted us to investigate OE stem
463 cell dynamics during nasal development.
464
465 We re-clustered the OPPs and GBCs characterized above and found that they
466 segregated into two distinct clusters (Fig. 6A). One cluster represented OPPs,
467 which peaked at embryonic day 10.5 (E10.5) and rapidly declined after E12.5,
468 whereas the other cluster comprised GBCs, which emerged at E12.5 and
469 persisted until E18.5 (Fig. 6B). This temporal transition aligns with the
470 established model of olfactory neurogenesis (Packard et al., 2011; Kim et al.,
471 2023), in which GBCs arise prior to horizontal basal cells (HBCs) and represent
472 predominant stem cell pool at embryonic stages. Both two clusters maintained
473 an undifferentiated state with expression of canonical olfactory stemness
474 markers *Sox2* and *Pax6* (Schwob, J. E. et al., 2017), and shared molecular
475 features related to DNA replication and cell cycle regulation (Fig. 6C and 6D).
476 However, GBCs exhibited high expression of late-stage olfactory stemness
477 markers *Ascl1* and *Kit*, which were minimally expressed in OPPs (Fig. 6C).
478 Differential gene expression (DGE) analysis revealed striking transcriptional
479 differences between OPPs and GBCs (Fig. 6D). OPPs specifically expressed
480 a set of previously uncharacterized genes, including *Sall4*, *Mest*, *Igf2bp1*, and
481 *Car14* (Fig. S10A). Notably, *Car14*, whose deficiency has been linked to liver

482 fibrosis (Qian et al., 2022), showed specific co-localization with *Sox2* in the
483 E11.5 OE by smFISH (Fig. 6E), suggesting a role in olfactory stem cell
484 regulation. In contrast, GBCs specifically expressed *Lgr5*, a known adult GBC
485 marker (Chen et al., 2014), along with other uncharacterized genes such as
486 *Tmprss4*, *Jag2* and *Runx1* (Fig. S10A). *Lgr5* expression in *Ascl1*$^{+}$ GBCs at
487 E14.0 was further validated by smFISH (Fig. 6E). Gene ontology (GO) analysis
488 revealed that OPPs-enriched genes were associated with epithelial cell
489 proliferation and Wnt signaling, whereas GBCs-enriched genes were linked to
490 Notch signaling and glial cell differentiation (Fig. 6D). SCENIC analysis
491 identified distinct regulons, including *Tcf7l1* in OPPs and *Tcf4* in GBCs (Fig.
492 S10B and S10C).
493
494 To further dissect heterogeneity of GBCs, we extended the single-cell timeline
495 of nasal development by integrating our mNEDCA dataset with published
496 postnatal datasets (Horgue et al., 2022; Ualiyeva et al., 2024; Yang et al., 2024)
497 spanning P19 to adult (P36W). Based on transcriptional features, GBCs were
498 classified into four subgroups with continuous developmental relationships (Fig.
499 6F). GBCs1, enriched for *Igf2bp1* and *Pak3* and associated with chromatin
500 remodeling and heterochromatin formation, may represent transitional cells
501 bridging OPPs and specialized GBCs (Fig. 6G and S10D). Prenatally, GBCs2
502 expressed *Dlx5* and *Sox21*, linked to axon guidance and sensory organ
503 morphogenesis, whereas GBCs3 expressed *Foxg1* and *Nfib*, associated with
504 neuronal fate commitment and gland development (Fig. 6G and S10D). These
505 two clusters corresponded to the "active" GBC states described in adult
506 neurogenesis (Schwob, James E et al., 2017). Postnatally, GBCs4, expressing
507 *Atp5o* and *Klf4* and enriched for pathways including negative regulation of
508 ERK1/2 signaling and modulation of endopeptidase activity, emerged as a
509 mature population (Fig. 6G and S10D and Table S8). Pseudotime analysis
510 confirmed a developmental trajectory from GBCs1 to active GBCs2/3, and
511 ultimately to the homeostatic GBCs4 state (Fig. S10E–S10G).
512
513 Collectively, we delineate the dynamic transcriptional landscape of olfactory
514 epithelial stem cells from E10.5 to adulthood, identifying novel markers that

515 distinguish OPPs from GBCs during embryogenesis and refining our
516 understanding of GBC heterogeneity and maturation.
517
518 **Discussion**
519 In this study, we presented a high-resolution temporal single-cell RNA
520 sequencing (scRNA-seq) atlas of mouse nasal development, profiling 183,247
521 cells from 20 embryos spanning embryonic day (E)10.5 to E18.5. We defined
522 seven major cell classes and 52 subtypes, uncovered a series of previously
523 unrecognized molecular markers, and identified rare or uncharacterized cell
524 populations. Cell–cell communication analysis revealed critical niche-derived
525 signals regulating respiratory epithelium (RE) progenitor cells maintenance,
526 which guided the establishment of an in vitro RE progenitor cells culture system.
527 Using this platform, we reconstructed the differentiation trajectory of RE
528 lineages and demonstrated that Foxa1 functions as a key driver promoting
529 nasal RE progenitors toward a ciliated epithelial fate. Furthermore, we
530 delineated the transcriptional dynamics of olfactory epithelium (OE) stem cells
531 from E10.5 through adulthood. The resulting mouse nasal embryonic
532 development cell atlas (mNEDCA) offered a valuable reference for nasal
533 development and regenerative medicine, particularly for stem cell-based
534 strategies to restore nasal structure and function.
535
536 The nose serves as both a critical respiratory gateway and a sensory organ,
537 and its development involves a complex interplay of diverse cell populations.
538 The temporal resolution and deep transcript coverage of mNEDCA enabled
539 systematic annotation of developmental stage–specific cell states. We
540 performed unbiased clustering for each developmental stage, annotated
541 clusters based on previously known markers and newly identified specific
542 genes, which were validated them by smFISH or immunofluorescence in the
543 context of anatomical structures. This approach uncovered novel markers,
544 including *Cyp4v3* as an OE-enriched gene and *Car14* as an early OE stem cell
545 associated marker. We also identified previously unreported cell types, such as
546 *Sftpc*$^{+}$ ciliated cell subset at late gestation and mesenchymal progenitor cells
547 (MPCs) that serve as intermediates during nasal mesenchyme differentiation.

Functional characterization of these genes and cell types will expand current understanding of nasal epithelial and mesenchymal development.

Among diverse cell populations, the epithelium plays a dominant functional role in nasal function and patterning. Analogous to other developing organs (Ribatti and Santoiemma, 2014; Le Guen et al., 2015; El Agha and Thannickal, 2023), nasal morphogenesis is shaped by reciprocal epithelial–mesenchymal interactions mediated by BMP, FGF, retinoic acid, and sonic hedgehog (SHH) signaling (LaMantia et al., 2000; Maier et al., 2010; Maier et al., 2011; Forni et al., 2013). Consistently, mNEDCA delineated multilayered inductive networks involving BMP, FGF, NOTCH, and WNT pathways across distinct cell populations. Notably, compared with other epithelial cell subtypes, RE development relies more heavily on its own autocrine signals. We identified FGF, NOTCH, and WNT circuits as core regulators of RE progenitor homeostasis and leveraged this insight to establish a chemically defined culture system. Within this context, we functionally validated *Foxa1* as a driver of RE differentiation toward the ciliated lineage. Although *Foxa1* expression in RE has been reported (Besnard et al., 2004), its developmental role was unclear. Our data indicate that *Foxa1* promotes ciliogenic programs, raising the possibility that *Foxa1* deficiency in vivo could impair mucociliary clearance and epithelial barrier integrity. Given the established role of *Foxa1* as a pioneer factor in lung epithelial development (Wan et al., 2005; Paranjapye et al., 2020), together with the identification of *Sftpc*$^{+}$ ciliated subtypes in the nasal RE, suggests conserved mechanisms across the upper and lower respiratory tract. The RE progenitor system described here provides a promising platform for dissecting RE cell fate regulation and for isolating corresponding human stem cells for therapeutic applications in nose diseases.

In the OE, defining the precise stem cell populations remains an area of active debate. Globose basal cells (GBCs) and horizontal basal cells (HBCs) are two widely recognized candidates (Iwai et al., 2008; Fletcher et al., 2017). Our dataset captured both populations, as well as olfactory placode progenitors (OPPs) that give rise to diverse OE epithelial cell types. In agreement with

previous studies (Packard et al., 2011; Kim et al., 2023), GBCs emerged earlier and were more abundant than HBCs, suggesting a potential primary role for GBCs in lineage specification during embryogenesis. We also resolved GBC heterogeneity across development and identified distinct markers separating GBCs from OPPs. Integration with postnatal datasets (Horgue et al., 2022; Ualiyeva et al., 2024; Yang et al., 2024) bridged embryonic and adult programs, although full reconstruction of OE lineages remains challenging due to plasticity and mixed origins. Definitive resolution will require lineage-tracing initiated at E9.5 or earlier and regionally targeted scRNA-seq from the frontonasal process.

Despite these findings, several limitations for mNEDCA should be considered. Cell coverage of mNEDCA at late developmental stages is low relative to the total nasal cellularity. This may lead to underrepresentation of rare cell types, such as Grueneberg ganglion which appear around E16.0 and contain less than 500 cells during embryogenesis (Fuss et al., 2005). Whole-tissue dissociation and droplet-based capture may bias against specialized neurons, including those of the septal organ. The absence of spatial transcriptomic information also limited discrimination of anatomically adjacent but transcriptionally similar populations like cells in septal organ, VNO and OE. Future integration of spatially resolved and region-specific profiling will refine the spatiotemporal architecture of nasal development. Moreover, although our analyses focused on epithelial and mesenchymal compartments, immune, endothelial, and neural crest–derived cells also contribute to morphogenesis and merit deeper exploration. Nevertheless, the mNEDCA provides a valuable resource to explore cellular heterogeneity, lineage dynamics, and regulatory networks during nasal embryogenesis, and offers novel insights into epithelial stem cell biology with implications for regenerative medicine.

MATERIALS AND METHODS

614

615 **Animals**

616 All animal experiments were performed in accordance with the Guide for the
617 Care and Use of Animals Protocol (AUCP, GZLAB-AUCP-2024-10-A03) and
618 approved by the Animal Ethics Committee of Guangzhou Laboratory. Mice were
619 housed in a specific pathogen-free (SPF) environment under a 12-h light-dark
620 cycle in the animal facility of Guangzhou National Laboratory, where the
621 temperature was controlled at 18–23 °C and humidity was maintained at 40%–
622 60%. Wild-type ICR mice were purchased from Charles River Laboratories
623 (License number: SCXK (Yue) 2022-0063).

624

625 **Mouse embryonic nasal sample collection and dissociation**

626 Timed-pregnant female ICR mice were euthanized by cervical dislocation at
627 various embryonic days (E10.5 to E18.5) at 24-h intervals. The embryos were
628 collected from the uterus, and nasal tissue was carefully dissected under a
629 stereomicroscope and washed twice with cold PBS for single-cell suspension.
630 The tissues were digested in 10 U/mL Papain (Worthington, LS003126) for
631 5 min at 37 °C, followed by mincing approximately 50 times to facilitate further
632 dissociation. Subsequently, 100 U/mL DNase I (Worthington Biochemicals,
633 LS006343) was added and the mixture was incubated for an additional 5–25
634 min. The enzymatic reaction was then terminated with 10% fetal bovine serum
635 (FBS, NTC, #SFBE), followed by supplementation with 20 U/mL DNase I to
636 ensure complete digestion of genomic DNA. After enzymatic digestion, cells
637 were filtered through 40-μm cell strainers (Falcon, 352360) on ice and
638 centrifuged at 300 × *g* for 5 min at 4 °C. Cell counting and viability assessments
639 were performed via trypan blue staining. The resulting cells were collected into
640 PCR tubes for subsequent single-cell library preparation and sequencing.

641

642 **scRNA-seq library construction and sequencing**

Single-cell suspensions from E10.5 to E18.5 embryos were loaded onto 10× Genomics Chromium Single Cell 3' v3.1 system to generate single-cell gel beads-in-emulsion (GEMs). After incubation, the GEMs were disrupted to release the encapsulated single cells, and cDNA was subsequently synthesized and amplified via PCR. For library preparation, 25% of total cDNA (10 μL) was used to construct 3' gene expression libraries. These libraries were then purified using SPRIselect beads (Beckman, B23319) to remove residual remaining reagents and contaminants, ensuring high-quality library preparation. Quality control of the libraries was performed using the Qsep100 system (Bioptic) for size distribution and Qubit 4.0 fluorometer for concentration quantification of the libraries. The sequencing of the libraries was carried out on DNBSEQ-T7 system (MGI), utilizing a paired-end mode (PE150) with a total output of 120 Gb of data.

Preprocessing of scRNA-seq data

Raw FASTQ files from single-cell libraries generated using an MGI DNBSEQ-T7 system were processed as follows. Initial quality assessment was performed with fastp (v0.20.0). For sequence trimming, Trim Galore (v0.6.6) (integrated with Cutadapt) was utilized to perform hard-trimming, with the R1 and R2 reads were trimmed to 28 bp and 98 bp respectively (--hardtrim5). The processed clean reads were then aligned to the mm10 reference genome with mouse gene annotation (vM21) using STARsolo module within STAR (v2.7.6a) (Dobin et al., 2013). Alignment parameters were as follows: --soloType Droplet --soloFeatures Gene --soloCBstart 1 --soloCBlen 16 --soloUMIstart 17 --soloUMIlen 12.

The Python library Scanpy (v1.6.0) (Wolf et al., 2018) was used to read and integrate the combined gene-barcode matrices of these samples. To ensure a high-quality cell atlas for downstream analysis, stringent quality control (QC)

was performed based on the number of detected genes (nGenes), unique molecular identifiers (UMIs) and the percentage of mitochondrial genes (percent.mito). To account for both technical and biological variability across stages and replicates, sample-specific filtering thresholds were applied (see Table S1 for details). Generally, low-quality cells with high mitochondrial content were excluded. Furthermore, potential doublets were identified and removed using Scrublet (v1.0) (Wolock et al., 2019) with scanpy.pp.scrublet. Following these filtering steps, a total of 183,247 high-quality cells were retained, with a median of 3,777 detected genes and 12,822 UMIs per cell.

Cell cluster identification

To minimize technical variability, major cell clusters were identified for each sample separately prior to dataset integration. Raw counts were normalized to 10,000 counts per cell and log-transformed. The top 3,000 highly variable genes (HVGs) were selected for downstream analysis. Principal component analysis (PCA) was performed on these HVGs, and the first 30 principal components were used to construct a k-nearest-neighbor (KNN) graph (n_neighbors = 10). Uniform Manifold Approximation and Projection (UMAP) was employed for visualization. Cell clusters were identified using the Leiden graph-clustering algorithm. To characterize cluster identities, differentially expressed genes (DEGs) were identified using the Wilcoxon rank-sum test. Significant marker genes were defined by a Benjamini–Hochberg adjusted *P*-value < 0.01 and a log fold change ($\log_2$FC) ≥ 0.25.

To achieve a high-resolution and biologically accurate characterization of the cellular landscape, a hierarchical annotation strategy was employed based on canonical markers curated from published literature (Table S2). Initial broad clusters were annotated by cross-referencing the expression of these markers, and their specificity was verified using dot plots and UMAP feature plots. An iterative sub-clustering strategy was then performed to refine annotations. First,

clusters expressing proliferation-related genes (e.g., *Top2a*, *Mki67*) were labelled with the suffix "_prolif" (e.g., "Chondrocyte_prolif"). Second, heterogeneous populations were further stratified through re-clustering. For example, ciliated cells were subdivided into "Ciliated cells1_Sftpc−" and "Ciliated cells2_Sftpc+" subpopulations based on differential expression of *Sftpc* and *Cdhr3*. Third, low-abundance populations, including *Gnrh1*$^{+}$ neurons, *Prokr2*$^{+}$ terminal neurons, and *Sox10*$^{+}$/*Foxd3*$^{+}$ neural crest cells, were identified after dataset integration to improve detection sensitivity. This process resulted in 52 distinct cellular clusters.

Additionally, gene ontology (GO) enrichment analysis for DEGs associated with each cluster was performed using the clusterProfiler R package (Yu et al., 2012) in R.

Data Integration

To characterize the global cellular landscape and the epithelial compartment, dimensionality reduction was performed based on feature selection. HVGs were identified with expression thresholds (min_mean = 0.0125, max_mean = 3, and min_disp = 0.5) to capture biological variability. PCA was conducted on these HVGs, and the top 40 PCs for global atlas or 30 PCs for epithelial subset were retained. The neighborhood graph was then constructed (n_neighbors = 10), followed by UMAP visualization.

For the mesenchymal lineage, Harmony (Korsunsky et al., 2019) was used to correct for batch effects. The top 2,000 HVGs were selected with (batch_key = “Batch”). After computing the top 30 PCs, batch-corrected embeddings were generated by Harmony and used for neighborhood graph construction and UMAP visualization.

For several regions of neurogenic and non-neurogenic epithelial cells, batch

correction was performed using BBKNN (Batch-Balanced k-Nearest Neighbors) algorithm (Polanski et al., 2020). The top 2,000 HVGs were identified using batch-aware selection, followed by PCA (30 components) and BBKNN correction. To visualize continuous developmental trajectories, PHATE (Potential of Heat-diffusion for Affinity-based Trajectory Embedding) (Moon et al., 2019) was applied. PHATE embeddings of respiratory epithelial cells were generated with parameters (n_components = 2, knn = 40, gamma = 0.3), optimized to preserve global trajectory structures.

Pseudo-bulk RNA analysis

Pseudo-bulk RNA expression profiles were generated by aggregating single-cell raw counts corresponding to each time point. Counts per million (CPM) normalization followed by log transformation was performed. PCA was performed on the log-CPM matrix using prcomp function, and the first two principal components were extracted for visualization. To model temporal gene expression dynamics, a smooth curve was fitted to the aggregated profiles using the principal_curve function from the R package princurve (v2.1.6). Subsequently, the PCA scatter plots with overlaid fitted curves were visualized using ggplot2 (v3.4.0).

RNA velocity analysis

To infer directional state transitions, spliced and unspliced RNA transcripts were quantified for each sample using the STARsolo algorithm with the Velocyto option enabled. RNA velocity was estimated for mesenchymal and epithelial populations using scVelo (v0.2.3) (Bergen et al., 2020). Specifically, normalized moments of spliced and unspliced counts were calculated using 30 principal components and 20 nearest neighbors. The dynamical model was then applied to recover transcriptional kinetics, and RNA velocity was subsequently estimated in dynamical mode. A velocity graph was then constructed using 20 nearest neighbors, and velocity vectors were projected onto the corresponding

low-dimensional embeddings for visualization.

Trajectory inference

For mesenchymal trajectory inference, Partition-based Graph Abstraction (PAGA) (Wolf et al., 2019) was applied to reconstruct transitions between clusters. In this framework, edge weights represent connectivity strengths inferred from velocity-based transitions. Developmental progression was further evaluated by diffusion pseudotime (DPT) analysis.

For the respiratory epithelium, PAGA analysis was performed following the same strategy used for mesenchymal cells. In addition, Monocle2 (Qiu et al., 2017) was used to independently reconstruct the trajectory of respiratory epithelium cells. Specifically, the top 2,000 HVGs were selected to capture relevant transcriptional variability. Dimensionality reduction was conducted using the DDRTree algorithm, followed by cell ordering to define lineage relationships.

To further investigate the temporal dynamics of GBC subtypes, the dataset in this study was integrated with three published nasal epithelium datasets from GEO: P19 from GSE224604 (Yang et al., 2024), P8W from GSE185168 (Horgue et al., 2022), and P11W-P36W from GSE245074 (Ualiyeva et al., 2024). After integration, Monocle2 was applied to construct trajectories of GBC subtypes using 2,000 HVGs.

TF activity inference

Regulon inference and activity analysis were performed using the pySCENIC framework (v0.11.0) (Aibar et al., 2017) to identify transcription factor (TF)-centered regulatory programs across defined cell subpopulations. The analysis was conducted on a filtered expression matrix comprising 6,000 HVGs. First, co-expression relationships between TFs and potential target genes were

inferred using the GRNBoost2 algorithm with mouse TFs. The resulting TF-target adjacencies were grouped into co-expression modules. To obtain high-confidence regulons, cis-regulatory motif enrichment analysis was performed using prune2df based on the mm10 motif databases. Only TF-target interactions supported by significant motif enrichment (normalized Enrichment Score, NES > 3.0) were retained.

Regulatory activity at the single-cell level was quantified using AUCell. To improve the robustness, several filtering steps were applied: (i) TFs with low expression or activity (mean expression < 0.1) were excluded; (ii) regulons showing no activity across cell groups were removed; and (iii) regulons with motif enrichment NES > 3 were retained for downstream analysis. The final mean AUCell activity matrix was visualized using the ComplexHeatmap (v2.16.0) R package, with hierarchical clustering performed using the ward.D2 method to reveal cell-type-specific regulatory patterns.

Cell-cell interaction analysis

To characterize the intercellular communication landscape during mouse nasal development, the CellChat framework (v1.6.1) (Jin et al., 2021) was applied. Interactions were inferred based on the CellChatDB.mouse ligand-receptor database. Overexpressed ligands and receptors in each cell group were first identified, after which communication probabilities between cell groups were computed using a permutation-based approach implemented in CellChat. To ensure statistical robustness, only cell groups containing at least 10 cells were included in the analysis. Pathway-level communication probabilities were subsequently calculated by aggregating individual ligand–receptor pairs. To focus on high-confidence interactions and minimize redundancy, only ligand–receptor pairs with a communication probability greater than 0.01 were retained. When multiple interactions were detected between the same sender–receiver pair, only the interaction with the highest probability was kept for visualization.

822 The overall signaling strengths and specific ligand-receptor interactions across
823 subpopulations were visualized using bubble plots and circle plots.
824
825 **Bulk RNA library preparation and sequencing**
826 Total RNA was extracted using TRIzol Reagent (MRC, TR118) following the
827 manufacturer's instructions. Subsequently, sequencing libraries were
828 constructed using the VAHTS mRNA-seq v2 Library Prep Kit for Illumina
829 (Vazyme, NR605). Library sequencing was performed on an Illumina NovaSeq
830 X Plus platform (Annoroad Gene Technology).
831
832 **Bulk RNA-seq analysis**
833 The paired-end sequenced reads were aligned to a transcriptome index
834 generated from the GENCODE transcriptome annotation (M13) using Bowtie2,
835 and transcript quantification was performed with RSEM (Li and Dewey, 2011).
836 The resulting gene expression profiles were output in the *gene.results* file. Raw
837 read counts were used for differential expression analysis, while TPM values
838 were used for expression visualization and comparison. Differentially
839 expressed genes (DEGs) were identified using edgeR within the
840 R/Bioconductor framework (v3.6.1), applying a false discovery rate (FDR) <
841 0.05 and an absolute $\log_2$ fold change cutoff. GO enrichment analysis was
842 performed with DEGs using the R package clusterProfiler, with FDR correction
843 applied for multiple testing. GO terms with an adjusted *P*-value < 0.05 were
844 considered significantly enriched. Figures were generated using the ggplot2
845 package (v3.3.2).
846
847 **Primary RE progenitor cells cultures**
848 Timed-pregnant ICR mice at E11.5 were euthanized by cervical dislocation.
849 Embryos were collected and washed twice with cold PBS. Nasal tissues were
850 carefully dissected from embryos under a stereomicroscope using fine forceps.
851 Dissected tissues were incubated in 20U/mL Dispase II (Gibco, #17105-041)

852 for 10 min to facilitate separation of the epithelial layer from the underlying
853 mesenchyme. The respiratory epithelial (RE) progenitor region was identified
854 based on FGF8 immunostaining in E11.5 nasal tissue sections, as previously
855 described (Kawauchi et al., 2005). The *Fgf8*$^{+}$ RE progenitor region was then
856 microdissected using insulin syringe needles (BD, #328421). The isolated
857 epithelium was subsequently fragmented into small clusters by treatment with
858 10 U/mL Papain (Worthington, LS003126) at 37 °C for 1 min, and terminated
859 by adding an equal volume of 10% FBS. Cell clusters were embedded in
860 Matrigel (Corning, #354234) and cultured in ALL medium. Cultures were
861 maintained at 37 °C in a humidified with 5% CO2 atmosphere, with medium
862 refreshed every 48 h in 24-well plate.
863
864 **Foxa1 overexpression**
865 The full-length coding sequence (CDS) of mouse *Foxa1* was amplified by PCR
866 from cDNA derived from mouse lung tissue, and cloned into the pMXs
867 expression vector. Retroviruses were produced in Plat-E cells via
868 polyethylenimine (PEI)-mediated transfection. Briefly, 7.5 × 10^6 Plat-E Cells
869 were seeded in 10-cm dish and cultured in medium containing 10% FBS for 12-
870 18 h before PEI transfection. For transfection, 20 μg plasmid DNA was mixed
871 with 40 μL PEI reagent (#MW40000, YEASEN) in Opti-MEM and incubated for
872 15 min at room temperature. The mixture was then added to the Plat-E cells,
873 and the medium was replaced 10 h post-transfection. Retroviral supernatants
874 were harvested 48 h post-transfection.
875
876 For 3D culture, 80 μL of ice-cold Matrigel was first added to each well of a 48-
877 well plate, evenly covering the well bottom, and allowed to solidify at 37 °C for
878 20 min. Subsequently, 400 μL of the cell–virus mixture was added to the
879 Matrigel-coated wells and incubated for 16 h at 37 °C. Non-viable cells were

880 then removed by aspiration, followed by addition of a 60 μL Matrigel overlay
881 and solidification at 37°C for 20 min. Cultures were then maintained in ALL
882 medium, with medium changes every 48 h.
883
884 **Single-molecule fluorescence in situ hybridization (smFISH)**
885 SmFISH was performed following the protocol as previously described (Cao et
886 al., 2023). Tissue sections (10 μm) were cut using a Leica CM3050S cryostat
887 at –20 °C, and mounted onto adhesive glass slides (CITOTEST, #80312-3161).
888 Sections were fixed in 4% paraformaldehyde (PFA) in PBS for 10 min at room
889 temperature, washed three times with PBS (5 min each), and then immersed
890 in 70% (vol./vol.) ethanol for at least 1 h at room temperature.
891
892 The unlabeled gene-specific primary probes were synthesized by Sangon
893 Biotech (China). Secondary FLAP probes, conjugated with Cy3 or Cy5
894 fluorophores via 5'-amino modifications, were purchased from Thermo Fisher
895 Scientific (China). The sequences of all probes are provided in Table S9.
896
897 For in vitro pre-annealing, a reaction mixture containing 8.5 μL primary probe
898 mix, 0.5 μL secondary FLAP probe (Cy3 or Cy5), and 1 μL 10×NEB 3 buffer
899 was prepared on ice, followed by gentle pipetting to mix. The mixture was
900 subjected to thermal cycling with the following program: 85°C for 3 min; cooling
901 to 65 °C at –1 °C/s and holding for 3 min; further cooling to 25 °C at –0.1 °C/s
902 and incubating for 5 min. After cycling, the mixture was gently mixed by
903 pipetting without vortexing.
904
905 Hybridization buffer containing 10% formamide (DFA) was prepared in a fume
906 hood. The pre-annealed probe duplexes were diluted 1:50 (v/v) in the
907 hybridization buffer to a final working concentration of 3.2 nM for subsequent in

908 situ hybridization. For combined smFISH and immunofluorescence staining,
909 mouse monoclonal anti-E-cadherin (CDH1, 1:200; BD Transduction
910 Laboratories, 610181) was added into diluted probe-hybridization buffer. The
911 tissue sections on slides were outlined with a PAP pen, and Wash Buffer A (WA,
912 Biosearch Technologies, #SMF-WA1-60) was added dropwise to the circled
913 area for rehydration at room temperature for 10 min. The WA was then carefully
914 removed, and the diluted probe-hybridization buffer with primary antibody was
915 added dropwise onto each section individually. The slides were placed in a
916 humidity-controlled chamber and incubated at 37 °C for 16 h in the dark. After
917 hybridization, slides were washed twice by pre-warmed Wash Buffer A with
918 Alexa Fluor-conjugated donkey anti-mouse secondary antibody (488, 1:400,
919 Thermo Fisher) (37°C, 30 min each), then stained with 200 ng/mL DAPI in
920 Wash Buffer B (Biosearch Technologies, #SMF-WB1-20) for 5 min, and given
921 a final wash with Wash Buffer B. Sections were mounted with 50-100 μL anti-
922 fade medium under coverslips, with edges sealed using clear nail polish.
923
924 Confocal images were acquired using Olympus IXplore SpinSR confocal
925 microscope. Image processing including brightness/contrast adjustment,
926 pseudo-coloring, and z-stack alignment was performed uniformly across
927 datasets using Adobe Photoshop CC 2020 and Fiji/ImageJ software.
928
929 **Immunofluorescence**
930 Heads from ICR mouse embryos at embryonic days 11.5, 14.0 and 18.0 (E11.5,
931 E14.0, and E18.0) were dissected and fixed in 4% paraformaldehyde (PFA) for
932 16 h. Following fixation, the samples were dehydrated overnight in 30%
933 sucrose at 4 °C. The head tissue was embedded in OCT compound (Sakura,
934 #4583) and cryosectioned into 10 μm-thick sections. Sections were mounted
935 onto adhesive glass slides and stored at 4 °C until further processing.
936

937 For immunofluorescence staining, sections were washed three times with PBS,
938 permeabilized with 0.5% Triton X-100 for 20 min, and then blocked at room
939 temperature for 1 h with blocking buffer (5% BSA in PBS). Following blocking,
940 section were incubated overnight at 4 °C with primary antibodies: rabbit
941 polyclonal anti-SFTPC (1:200, Invitrogen, PA5-102493) and mouse monoclonal
942 anti-acetylated-α-Tubulin(1:1000, Sigma, T7451). Subsequently, sections were
943 incubated with Alexa Fluor-conjugated donkey or goat anti-mouse or anti-rabbit
944 secondary antibodies (488/568, 1:400, Thermo Fisher) for 2 h at room
945 temperature. Nuclei were visualized with DAPI (Invitrogen, D1306) for nuclear
946 staining, and slides were mounted using appropriate anti-fade mounting media
947 (KeyGEN BioTECH, KGA1523-5). Images were captured using the Andor
948 Dragonfly 200 confocal microscope.
949
950 **Quantitative real-time PCR (qRT–PCR)**
951 Total RNA was isolated using TRIzol Reagent (MRC, TR118). Complementary
952 DNA (cDNA) was synthesized from 1 μg of RNA via reverse transcription with
953 dNTPs (TIANGEN, CD111-03), oligo (dT) 18 (TakaRa, 3806), RT Ace
954 (TOYOBO, TRT-101), RNase inhibitor (Promega, N2511) and 5×RT Buffer
955 (TOYOBO, TRT-101). The qRT–PCR was performed using an iTaq™ Universal
956 SYBR® Green Supermix (Bio-Rad #1725124) on a CFX Connect Real-Time
957 PCR System (Bio-Rad). *Gapdh* was used as the endogenous control. Relative
958 gene expression was calculated using the ΔΔCt method. All reactions were
959 performed in technical triplicate, with no-template controls included. For
960 statistical analysis, two-tailed unpaired Student's *t*-test were used for
961 comparisons between two groups, while ordinary one-way ANOVA followed by
962 Dunnett's post hoc test was used when involving multiple groups (GraphPad
963 Prism 8). Significance was defined as $P < 0.05$. All primer sequences are

provided in Table S10.

Data availability

scRNA-seq and bulk RNA-seq data are available in NCBI GEO database with accession number GSE304937 and GSE304339.

CRediT authorship contribution statement

Huan Chen: Methodology, Data analysis, Organoid culture, Manuscript writing. **Yingxiu Chen**: Methodology, Library generation, smFISH, Manuscript writing. **Mengjie Pan**: Methodology, Embryonic nose dissection. **Ziyu Feng**: Methodology, Nose tissue dissociation. **Baomei Cai**: Methodology, Library generation. **Yiyi Cheng**: Organoid culture. **Sihao Chen, Jiehong Deng, Xia Yao, Chunhua Zhou, Yunjing Du, Wei He, Ruifang Zhang, Yudong Fu, Shujuan Liu**: Technical and experimental support. **Lihui Lin, Shengyong Yu, Yuehong Yan, Duanqing Pei, Dajiang Qin, Jiekai Chen**: Advices. **Dajiang Qin, Jiekai Chen**: Funding acquisition. **Shangtao Cao**: Conceptualization, Manuscript writing, Funding acquisition, Supervision

Conflict of interest

The authors declare that they have no conflict of interest.

Acknowledgement

This research was supported by grants from the National Natural Science Foundation of China (82470704); Major Project of Guangzhou National Laboratory (GZNL2023A02005); the National Key R&D Program of China (2024YFA1802300); Science and Technology Planning Project of Guangdong Province, China (2023TQ07A630); Key Laboratory of Guangdong Higher Education Institutes (2021KSYS009); Guangzhou Key Laboratory of Biological Targeting Diagnosis and Therapy (202201020379); We also thank a lot for public instrument service center Guangzhou National Laboratory and the

support from the Guangzhou Branch of the Supercomputing Center of the Chinese Academy of Sciences.

REFERENCES

Aibar, S., Gonzalez-Blas, C.B., Moerman, T., Huynh-Thu, V.A., Imrichova, H., Hulselmans, G., Rambow, F., Marine, J.C., Geurts, P., Aerts, J., van den Oord, J., Atak, Z.K., Wouters, J., Aerts, S., 2017. SCENIC: single-cell regulatory network inference and clustering. Nat Methods 14(11), 1083-1086. https://doi.org/10.1038/nmeth.4463.

Akiyama, H., 2008. Control of chondrogenesis by the transcription factor Sox9. Mod Rheumatol 18(3), 213-219. https://doi.org/10.1007/s10165-008-0048-x.

Amato, E., Jr., Taroc, E.Z.M., Forni, P.E., 2024. Illuminating the terminal nerve: Uncovering the link between GnRH-1 neuron and olfactory development. J Comp Neurol 532(3), e25599. https://doi.org/10.1002/cne.25599.

Balmer, C.W., LaMantia, A.S., 2005. Noses and neurons: induction, morphogenesis, and neuronal differentiation in the peripheral olfactory pathway. Dev Dyn 234(3), 464-481. https://doi.org/10.1002/dvdy.20582.

Barraud, P., Seferiadis, A.A., Tyson, L.D., Zwart, M.F., Szabo-Rogers, H.L., Ruhrberg, C., Liu, K.J., Baker, C.V., 2010. Neural crest origin of olfactory ensheathing glia. Proc Natl Acad Sci U S A 107(49), 21040-21045. https://doi.org/10.1073/pnas.1012248107.

Bergen, V., Lange, M., Peidli, S., Wolf, F.A., Theis, F.J., 2020. Generalizing RNA velocity to transient cell states through dynamical modeling. Nat Biotechnol 38(12), 1408-1414. https://doi.org/10.1038/s41587-020-0591-3.

Berger, M., Bergers, G., Arnold, B., Hammerling, G.J., Ganss, R., 2005. Regulator of G-protein signaling-5 induction in pericytes coincides with active vessel remodeling during neovascularization. Blood 105(3), 1094-1101. https://doi.org/10.1182/blood-2004-06-2315.

Besnard, V., Wert, S.E., Hull, W.M., Whitsett, J.A., 2004. Immunohistochemical localization of Foxa1 and Foxa2 in mouse embryos and adult tissues. Gene Expr Patterns 5(2), 193-208. https://doi.org/10.1016/j.modgep.2004.08.006.

Beverdam, A., Meijlink, F., 2001. Expression patterns of group-I aristaless-related genes during craniofacial and limb development. Mech Dev 107(1-2), 163-167. https://doi.org/10.1016/s0925-4773(01)00450-6.

Bird, J.E., Daudet, N., Warchol, M.E., Gale, J.E., 2010. Supporting cells eliminate dying sensory hair cells to maintain epithelial integrity in the avian inner ear. J Neurosci 30(37), 12545-12556. https://doi.org/10.1523/JNEUROSCI.3042-10.2010.

Buiakova, O., Baker, H., Scott, J., Farbman, A., Kream, R., Grillo, M., Franzen, L., Richman, M., Davis, L., Abbondanzo, S., 1996. Olfactory marker protein (OMP) gene deletion causes altered physiological activity of olfactory sensory neurons. Proceedings of the National Academy of Sciences 93(18), 9858-9863.

Cao, S., Feng, H., Yi, H., Pan, M., Lin, L., Zhang, Y.S., Feng, Z., Liang, W., Cai, B., Li, Q., Xiong, Z., Shen, Q., Ke, M., Zhao, X., Chen, H., He, Q., Min, M., Cai, Q., Liu, H., Wang, J., Pei, D., Chen, J., Ma, Y., 2023. Single-cell RNA sequencing reveals the developmental program underlying proximal-distal patterning of the human lung at the embryonic stage. Cell Res 33(6), 421-433.

https://doi.org/10.1038/s41422-023-00802-6.
Cau, E., Casarosa, S., Guillemot, F., 2002. Mash1 and Ngn1 control distinct steps of determination and differentiation in the olfactory sensory neuron lineage. Development 129(8), 1871-1880. https://doi.org/10.1242/dev.129.8.1871.
Chen, B., Kim, E.H., Xu, P.X., 2009. Initiation of olfactory placode development and neurogenesis is blocked in mice lacking both Six1 and Six4. Dev Biol 326(1), 75-85. https://doi.org/10.1016/j.ydbio.2008.10.039.
Chen, M., Tian, S., Yang, X., Lane, A.P., Reed, R.R., Liu, H., 2014. Wnt-responsive Lgr5(+) globose basal cells function as multipotent olfactory epithelium progenitor cells. J Neurosci 34(24), 8268-8276. https://doi.org/10.1523/JNEUROSCI.0240-14.2014.
Cho, H.J., Shan, Y., Whittington, N.C., Wray, S., 2019. Nasal Placode Development, GnRH Neuronal Migration and Kallmann Syndrome. Front Cell Dev Biol 7, 121. https://doi.org/10.3389/fcell.2019.00121.
Chung, W.C., Linscott, M.L., Rodriguez, K.M., Stewart, C.E., 2016. The Regulation and Function of Fibroblast Growth Factor 8 and Its Function during Gonadotropin-Releasing Hormone Neuron Development. Front Endocrinol (Lausanne) 7, 114. https://doi.org/10.3389/fendo.2016.00114.
Cuschieri, A., Bannister, L.H., 1975. The development of the olfactory mucosa in the mouse: electron microscopy. J Anat 119(Pt 3), 471-498.
Deprez, M., Zaragosi, L.-E., Truchi, M., Becavin, C., Ruiz García, S., Arguel, M.-J., Plaisant, M., Magnone, V., Lebrigand, K., Abelanet, S., 2020. A single-cell atlas of the human healthy airways. American journal of respiratory and critical care medicine 202(12), 1636-1645.
Dietz, A., Senf, K., Neuhaus, E.M., 2025. Stem cell expression of CXCR4 regulates tissue composition in the vomeronasal organ. Journal of Cell Science 138(1), jcs263451.
Dobin, A., Davis, C.A., Schlesinger, F., Drenkow, J., Zaleski, C., Jha, S., Batut, P., Chaisson, M., Gingeras, T.R., 2013. STAR: ultrafast universal RNA-seq aligner. Bioinformatics 29(1), 15-21. https://doi.org/10.1093/bioinformatics/bts635.
Duggan, C.D., DeMaria, S., Baudhuin, A., Stafford, D., Ngai, J., 2008. Foxg1 is required for development of the vertebrate olfactory system. Journal of Neuroscience 28(20), 5229-5239.
Duittoz, A.H., Forni, P.E., Giacobini, P., Golan, M., Mollard, P., Negron, A.L., Radovick, S., Wray, S., 2022. Development of the gonadotropin-releasing hormone system. J Neuroendocrinol 34(5), e13087. https://doi.org/10.1111/jne.13087.
Eckler, M.J., McKenna, W.L., Taghvaei, S., McConnell, S.K., Chen, B., 2011. Fezf1 and Fezf2 are required for olfactory development and sensory neuron identity. J Comp Neurol 519(10), 1829-1846. https://doi.org/10.1002/cne.22596.
El Agha, E., Thannickal, V.J., 2023. The lung mesenchyme in development, regeneration, and fibrosis. J Clin Invest 133(14). https://doi.org/10.1172/JCI170498.
Fletcher, R.B., Das, D., Gadye, L., Street, K.N., Baudhuin, A., Wagner, A., Cole, M.B., Flores, Q., Choi, Y.G., Yosef, N., Purdom, E., Dudoit, S., Risso, D., Ngai, J., 2017. Deconstructing Olfactory Stem Cell Trajectories at Single-Cell Resolution. Cell Stem Cell 20(6), 817-830 e818. https://doi.org/10.1016/j.stem.2017.04.003.
Forni, P.E., Bharti, K., Flannery, E.M., Shimogori, T., Wray, S., 2013. The indirect role of fibroblast growth factor-8 in defining neurogenic niches of the olfactory/GnRH systems. J Neurosci 33(50), 19620-19634. https://doi.org/10.1523/JNEUROSCI.3238-13.2013.
Forni, P.E., Taylor-Burds, C., Melvin, V.S., Williams, T., Wray, S., 2011. Neural crest and ectodermal

1080 cells intermix in the nasal placode to give rise to GnRH-1 neurons, sensory neurons, and olfactory
1081 ensheathing cells. J Neurosci 31(18), 6915-6927. https://doi.org/10.1523/JNEUROSCI.6087-
1082 10.2011.
1083 Fujita, T., Azuma, Y., Fukuyama, R., Hattori, Y., Yoshida, C., Koida, M., Ogita, K., Komori, T., 2004.
1084 Runx2 induces osteoblast and chondrocyte differentiation and enhances their migration by
1085 coupling with PI3K-Akt signaling. J Cell Biol 166(1), 85-95. https://doi.org/10.1083/jcb.200401138.
1086 Fuss, S.H., Omura, M., Mombaerts, P., 2005. The Grueneberg ganglion of the mouse projects axons
1087 to glomeruli in the olfactory bulb. Eur J Neurosci 22(10), 2649-2654.
1088 https://doi.org/10.1111/j.1460-9568.2005.04468.x.
1089 Gokoffski, K.K., 2010. TGF-βs mediate feedback regulation of neurogenesis and gliogenesis in the
1090 mammalian olfactory epithelium. University of California, Irvine.
1091 Gong, Q., Chen, H., Farbman, A.I., 2009. Olfactory sensory axon growth and branching is influenced
1092 by sonic hedgehog. Dev Dyn 238(7), 1768-1776. https://doi.org/10.1002/dvdy.22005.
1093 Graziadei, G.M., Stanley, R., Graziadei, P., 1980. The olfactory marker protein in the olfactory system
1094 of the mouse during development. Neuroscience 5(7), 1239-1252.
1095 Gu, J., Dudley, C., Su, T., Spink, D.C., Zhang, Q.Y., Moss, R.L., Ding, X., 1999. Cytochrome P450 and
1096 steroid hydroxylase activity in mouse olfactory and vomeronasal mucosa. Biochem Biophys Res
1097 Commun 266(1), 262-267. https://doi.org/10.1006/bbrc.1999.1807.
1098 Hills, M.H., Ma, L., Fang, A., Chiremba, T., Malloy, S., Scott, A.R., Perera, A.G., Yu, C.R., 2024.
1099 Molecular, cellular, and developmental organization of the mouse vomeronasal organ at single
1100 cell resolution. Elife 13. https://doi.org/10.7554/eLife.97356.
1101 Hojo, H., Ohba, S., 2019. Insights into Gene Regulatory Networks in Chondrocytes. Int J Mol Sci
1102 20(24). https://doi.org/10.3390/ijms20246324.
1103 Horgue, L.F., Assens, A., Fodoulian, L., Marconi, L., Tuberosa, J., Haider, A., Boillat, M., Carleton, A.,
1104 Rodriguez, I., 2022. Transcriptional adaptation of olfactory sensory neurons to GPCR identity and
1105 activity. Nat Commun 13(1), 2929. https://doi.org/10.1038/s41467-022-30511-4.
1106 Iwai, N., Zhou, Z., Roop, D.R., Behringer, R.R., 2008. Horizontal basal cells are multipotent
1107 progenitors in normal and injured adult olfactory epithelium. Stem Cells 26(5), 1298-1306.
1108 https://doi.org/10.1634/stemcells.2007-0891.
1109 Jia, R., Meng, X., Chen, S., Zhang, F., Du, J., Liu, X., Yang, L., 2023. AAV-mediated gene-replacement
1110 therapy restores viability of BCD patient iPSC derived RPE cells and vision of Cyp4v3 knockout
1111 mice. Hum Mol Genet 32(1), 122-138. https://doi.org/10.1093/hmg/ddac181.
1112 Jin, S., Guerrero-Juarez, C.F., Zhang, L., Chang, I., Ramos, R., Kuan, C.H., Myung, P., Plikus, M.V.,
1113 Nie, Q., 2021. Inference and analysis of cell-cell communication using CellChat. Nat Commun 12(1),
1114 1088. https://doi.org/10.1038/s41467-021-21246-9.
1115 Katoh, H., Shibata, S., Fukuda, K., Sato, M., Satoh, E., Nagoshi, N., Minematsu, T., Matsuzaki, Y.,
1116 Akazawa, C., Toyama, Y., Nakamura, M., Okano, H., 2011. The dual origin of the peripheral olfactory
1117 system: placode and neural crest. Mol Brain 4, 34. https://doi.org/10.1186/1756-6606-4-34.
1118 Katreddi, R.R., Forni, P.E., 2021. Mechanisms underlying pre- and postnatal development of the
1119 vomeronasal organ. Cell Mol Life Sci 78(12), 5069-5082. https://doi.org/10.1007/s00018-021-
1120 03829-3.
1121 Katreddi, R.R., Taroc, E.Z.M., Hicks, S.M., Lin, J.M., Liu, S., Xiang, M., Forni, P.E., 2022. Notch signaling
1122 determines cell-fate specification of the two main types of vomeronasal neurons of rodents.
1123 Development 149(13), dev200448.

1124 Kaucka, M., Petersen, J., Tesarova, M., Szarowska, B., Kastriti, M.E., Xie, M., Kicheva, A., Annusver,
1125 K., Kasper, M., Symmons, O., Pan, L., Spitz, F., Kaiser, J., Hovorakova, M., Zikmund, T., Sunadome,
1126 K., Matise, M.P., Wang, H., Marklund, U., Abdo, H., Ernfors, P., Maire, P., Wurmser, M., Chagin, A.S.,
1127 Fried, K., Adameyko, I., 2018. Signals from the brain and olfactory epithelium control shaping of
1128 the mammalian nasal capsule cartilage. Elife 7. https://doi.org/10.7554/eLife.34465.
1129 Kawauchi, S., Beites, C.L., Crocker, C.E., Wu, H.H., Bonnin, A., Murray, R., Calof, A.L., 2004. Molecular
1130 signals regulating proliferation of stem and progenitor cells in mouse olfactory epithelium. Dev
1131 Neurosci 26(2-4), 166-180. https://doi.org/10.1159/000082135.
1132 Kawauchi, S., Shou, J., Santos, R., Hebert, J.M., McConnell, S.K., Mason, I., Calof, A.L., 2005. Fgf8
1133 expression defines a morphogenetic center required for olfactory neurogenesis and nasal cavity
1134 development in the mouse. Development 132(23), 5211-5223. https://doi.org/10.1242/dev.02143.
1135 Kim, B.R., Rha, M.S., Cho, H.J., Yoon, J.H., Kim, C.H., 2023. Spatiotemporal dynamics of the
1136 development of mouse olfactory system from prenatal to postnatal period. Front Neuroanat 17,
1137 1157224. https://doi.org/10.3389/fnana.2023.1157224.
1138 Kim, C.H., Park, H.W., Kim, K., Yoon, J.H., 2004. Early development of the nose in human embryos:
1139 a stereomicroscopic and histologic analysis. Laryngoscope 114(10), 1791-1800.
1140 https://doi.org/10.1097/00005537-200410000-00022.
1141 Kitagaki, J., Ueda, Y., Chi, X., Sharma, N., Elder, C.M., Truffer, E., Costantini, F., Lewandoski, M.,
1142 Perantoni, A.O., 2011. FGF8 is essential for formation of the ductal system in the male reproductive
1143 tract. Development 138(24), 5369-5378. https://doi.org/10.1242/dev.051888.
1144 Korsunsky, I., Millard, N., Fan, J., Slowikowski, K., Zhang, F., Wei, K., Baglaenko, Y., Brenner, M., Loh,
1145 P.R., Raychaudhuri, S., 2019. Fast, sensitive and accurate integration of single-cell data with
1146 Harmony. Nat Methods 16(12), 1289-1296. https://doi.org/10.1038/s41592-019-0619-0.
1147 Krolewski, R.C., Packard, A., Jang, W., Wildner, H., Schwob, J.E., 2012. Ascl1 (Mash1) knockout
1148 perturbs differentiation of nonneuronal cells in olfactory epithelium. PLoS One 7(12), e51737.
1149 https://doi.org/10.1371/journal.pone.0051737.
1150 Krolewski, R.C., Packard, A., Schwob, J.E., 2013. Global expression profiling of globose basal cells
1151 and neurogenic progression within the olfactory epithelium. J Comp Neurol 521(4), 833-859.
1152 https://doi.org/10.1002/cne.23204.
1153 Kusumoto, T., Yotsukura, M., Asakura, T., Namkoong, H., Ogawa, T., Hegab, A.E., Nakatake, Y., Oda,
1154 M., Saito, F., Kamata, H., Hamamoto, J., Okamori, S., Seki, M., Suzuki, Y., Hasegawa, N., Asamura,
1155 H., Watanabe, H., Ko, M.S.H., Ieda, M., Fukunaga, K., Ishii, M., 2025. Induced lung epithelial-like
1156 cells derived by direct reprogramming rescue influenza virus-induced lung injury in mice. Biochem
1157 Biophys Res Commun 778, 152384. https://doi.org/10.1016/j.bbrc.2025.152384.
1158 LaMantia, A.S., Bhasin, N., Rhodes, K., Heemskerk, J., 2000. Mesenchymal/epithelial induction
1159 mediates olfactory pathway formation. Neuron 28(2), 411-425. https://doi.org/10.1016/s0896-
1160 6273(00)00121-5.
1161 Le Guen, L., Marchal, S., Faure, S., de Santa Barbara, P., 2015. Mesenchymal-epithelial interactions
1162 during digestive tract development and epithelial stem cell regeneration. Cell Mol Life Sci 72(20),
1163 3883-3896. https://doi.org/10.1007/s00018-015-1975-2.
1164 Li, B., Dewey, C.N., 2011. RSEM: accurate transcript quantification from RNA-Seq data with or
1165 without a reference genome. BMC Bioinformatics 12, 323. https://doi.org/10.1186/1471-2105-
1166 12-323.
1167 Lin, J.M., Mitchell, T.A., Rothstein, M., Pehl, A., Taroc, E.Z.M., Katreddi, R.R., Parra, K.E., Zuloaga,

1168 D.G., Simoes-Costa, M., Forni, P.E., 2022. Sociosexual behavior requires both activating and
1169 repressive roles of Tfap2e/AP-2epsilon in vomeronasal sensory neurons. Elife 11.
1170 https://doi.org/10.7554/eLife.77259.
1171 Ma, M., Grosmaitre, X., Iwema, C.L., Baker, H., Greer, C.A., Shepherd, G.M., 2003. Olfactory signal
1172 transduction in the mouse septal organ. J Neurosci 23(1), 317-324.
1173 https://doi.org/10.1523/JNEUROSCI.23-01-00317.2003.
1174 Maier, E., Nord, H., von Hofsten, J., Gunhaga, L., 2011. A balance of BMP and notch activity
1175 regulates neurogenesis and olfactory nerve formation. PLoS One 6(2), e17379.
1176 https://doi.org/10.1371/journal.pone.0017379.
1177 Maier, E., von Hofsten, J., Nord, H., Fernandes, M., Paek, H., Hebert, J.M., Gunhaga, L., 2010.
1178 Opposing Fgf and Bmp activities regulate the specification of olfactory sensory and respiratory
1179 epithelial cell fates. Development 137(10), 1601-1611. https://doi.org/10.1242/dev.051219.
1180 McIntyre, J.C., Titlow, W.B., McClintock, T.S., 2010. Axon growth and guidance genes identify
1181 nascent, immature, and mature olfactory sensory neurons. J Neurosci Res 88(15), 3243-3256.
1182 https://doi.org/10.1002/jnr.22497.
1183 Moon, K.R., van Dijk, D., Wang, Z., Gigante, S., Burkhardt, D.B., Chen, W.S., Yim, K., Elzen, A.V.D.,
1184 Hirn, M.J., Coifman, R.R., Ivanova, N.B., Wolf, G., Krishnaswamy, S., 2019. Visualizing structure and
1185 transitions in high-dimensional biological data. Nat Biotechnol 37(12), 1482-1492.
1186 https://doi.org/10.1038/s41587-019-0336-3.
1187 Murdoch, B., DelConte, C., Garcia-Castro, M.I., 2010. Embryonic Pax7-expressing progenitors
1188 contribute multiple cell types to the postnatal olfactory epithelium. J Neurosci 30(28), 9523-9532.
1189 https://doi.org/10.1523/JNEUROSCI.0867-10.2010.
1190 Nakano, Y., Kim, S.H., Kim, H.M., Sanneman, J.D., Zhang, Y., Smith, R.J., Marcus, D.C., Wangemann,
1191 P., Nessler, R.A., Banfi, B., 2009. A claudin-9-based ion permeability barrier is essential for hearing.
1192 PLoS Genet 5(8), e1000610. https://doi.org/10.1371/journal.pgen.1000610.
1193 Negishi, T., Mihara, N., Chiba, T., D'Armiento, J., Chada, K., Maeda, M., Igarashi, M., Imai, K., 2022.
1194 High mobility group AT-hook 2 regulates osteoblast differentiation and facial bone development.
1195 Biochem Biophys Res Commun 590, 68-74. https://doi.org/10.1016/j.bbrc.2021.12.093.
1196 Packard, A., Schnittke, N., Romano, R.A., Sinha, S., Schwob, J.E., 2011. DeltaNp63 regulates stem
1197 cell dynamics in the mammalian olfactory epithelium. J Neurosci 31(24), 8748-8759.
1198 https://doi.org/10.1523/JNEUROSCI.0681-11.2011.
1199 Paranjapye, A., Mutolo, M.J., Ebron, J.S., Leir, S.H., Harris, A., 2020. The FOXA1 transcriptional
1200 network coordinates key functions of primary human airway epithelial cells. Am J Physiol Lung Cell
1201 Mol Physiol 319(1), L126-L136. https://doi.org/10.1152/ajplung.00023.2020.
1202 Paronett, E.M., Bryan, C.A., Maynard, T.M., LaMantia, A.S., 2023. Identity, lineage and fates of a
1203 temporally distinct progenitor population in the embryonic olfactory epithelium. Dev Biol 495, 76-
1204 91. https://doi.org/10.1016/j.ydbio.2023.01.001.
1205 Parslow, V.R., Elmore, S.A., Cochran, R.Z., Bolon, B., Mahler, B., Sabio, D., Lubeck, B.A., 2024.
1206 Histology Atlas of the Developing Mouse Respiratory System From Prenatal Day 9.0 Through
1207 Postnatal Day 30. Toxicol Pathol 52(4), 153-227. https://doi.org/10.1177/01926233241252114.
1208 Perera, S.N., Williams, R.M., Lyne, R., Stubbs, O., Buehler, D.P., Sauka-Spengler, T., Noda, M.,
1209 Micklem, G., Southard-Smith, E.M., Baker, C.V.H., 2020. Insights into olfactory ensheathing cell
1210 development from a laser-microdissection and transcriptome-profiling approach. Glia 68(12),
1211 2550-2584. https://doi.org/10.1002/glia.23870.

1212 Polanski, K., Young, M.D., Miao, Z., Meyer, K.B., Teichmann, S.A., Park, J.E., 2020. BBKNN: fast batch
1213 alignment of single cell transcriptomes. Bioinformatics 36(3), 964-965.
1214 https://doi.org/10.1093/bioinformatics/btz625.
1215 Qian, J., Shen, Q., Zhang, T., Chen, J., Chen, L., Dong, Y., Yan, R., Chen, Z., 2022. Carbonic anhydrase
1216 14 protects the liver against the cytotoxicity of bile acids in a biliary bicarbonate umbrella-related
1217 manner. Life Sci 310, 121117. https://doi.org/10.1016/j.lfs.2022.121117.
1218 Qiu, X., Mao, Q., Tang, Y., Wang, L., Chawla, R., Pliner, H.A., Trapnell, C., 2017. Reversed graph
1219 embedding resolves complex single-cell trajectories. Nat Methods 14(10), 979-982.
1220 https://doi.org/10.1038/nmeth.4402.
1221 Ribatti, D., Santoiemma, M., 2014. Epithelial-mesenchymal interactions: a fundamental
1222 Developmental Biology mechanism. Int J Dev Biol 58(5), 303-306.
1223 https://doi.org/10.1387/ijdb.140143dr.
1224 Rodenburg, L.W., Metzemaekers, M., van der Windt, I.S., Smits, S.M.A., den Hertog-Oosterhoff,
1225 L.A., Kruisselbrink, E., Brunsveld, J.E., Michel, S., de Winter-de Groot, K.M., van der Ent, C.K.,
1226 Stadhouders, R., Beekman, J.M., Amatngalim, G.D., 2023. Exploring intrinsic variability between
1227 cultured nasal and bronchial epithelia in cystic fibrosis. Sci Rep 13(1), 18573.
1228 https://doi.org/10.1038/s41598-023-45201-4.
1229 Roskams, A.J., Cai, X., Ronnett, G.V., 1998. Expression of neuron-specific beta-III tubulin during
1230 olfactory neurogenesis in the embryonic and adult rat. Neuroscience 83(1), 191-200.
1231 https://doi.org/10.1016/s0306-4522(97)00344-8.
1232 Samee, N., Geoffroy, V., Marty, C., Schiltz, C., Vieux-Rochas, M., Levi, G., de Vernejoul, M.C., 2008.
1233 Dlx5, a positive regulator of osteoblastogenesis, is essential for osteoblast-osteoclast coupling.
1234 Am J Pathol 173(3), 773-780. https://doi.org/10.2353/ajpath.2008.080243.
1235 Schwob, J.E., Jang, W., Holbrook, E.H., Lin, B., Herrick, D.B., Peterson, J.N., Hewitt Coleman, J., 2017.
1236 Stem and progenitor cells of the mammalian olfactory epithelium: Taking poietic license. Journal
1237 of Comparative Neurology 525(4), 1034-1054.
1238 Schwob, J.E., Jang, W., Holbrook, E.H., Lin, B., Herrick, D.B., Peterson, J.N., Hewitt Coleman, J., 2017.
1239 Stem and progenitor cells of the mammalian olfactory epithelium: Taking poietic license. J Comp
1240 Neurol 525(4), 1034-1054. https://doi.org/10.1002/cne.24105.
1241 Senf, K., Nietzsche, S., Westermann, M., Neuhaus, E.M., 2025. Unraveling the Role of Ensheathing
1242 Cells and Perineural Fibroblasts in Olfactory Neurogenesis. Glia 73(12), 2407-2426.
1243 https://doi.org/10.1002/glia.70076.
1244 Shaker, T., Dennis, D., Kurrasch, D.M., Schuurmans, C., 2012. Neurog1 and Neurog2 coordinately
1245 regulate development of the olfactory system. Neural development 7(1), 28.
1246 Sokpor, G., Abbas, E., Rosenbusch, J., Staiger, J.F., Tuoc, T., 2018. Transcriptional and Epigenetic
1247 Control of Mammalian Olfactory Epithelium Development. Mol Neurobiol 55(11), 8306-8327.
1248 https://doi.org/10.1007/s12035-018-0987-y.
1249 Streit, A., 2004. Early development of the cranial sensory nervous system: from a common field to
1250 individual placodes. Dev Biol 276(1), 1-15. https://doi.org/10.1016/j.ydbio.2004.08.037.
1251 Suzuki, J., Osumi, N., 2015. Neural crest and placode contributions to olfactory development. Curr
1252 Top Dev Biol 111, 351-374. https://doi.org/10.1016/bs.ctdb.2014.11.010.
1253 Taroc, E.Z.M., Amato, E., Jr., Semon, A.M., Dolphin, N., Beck, B., Belin, S., Poitelon, Y., Forni, P.E.,
1254 2025. Shared Lineage, Distinct Outcomes: Yap and Taz Loss Differentially Impact Schwann and
1255 Olfactory Ensheathing Cell Development Without Disrupting GnRH-1 Migration. Glia 73(10),

2077-2097. https://doi.org/10.1002/glia.70057.
Taroc, E.Z.M., Katreddi, R.R., Forni, P.E., 2020. Identifying Isl1 Genetic Lineage in the Developing Olfactory System and in GnRH-1 Neurons. Front Physiol 11, 601923. https://doi.org/10.3389/fphys.2020.601923.
Tian, H., Ma, M., 2008. Differential development of odorant receptor expression patterns in the olfactory epithelium: a quantitative analysis in the mouse septal organ. Dev Neurobiol 68(4), 476-486. https://doi.org/10.1002/dneu.20612.
Treutlein, B., Brownfield, D.G., Wu, A.R., Neff, N.F., Mantalas, G.L., Espinoza, F.H., Desai, T.J., Krasnow, M.A., Quake, S.R., 2014. Reconstructing lineage hierarchies of the distal lung epithelium using single-cell RNA-seq. Nature 509(7500), 371-375. https://doi.org/10.1038/nature13173.
Tsukahara, T., Brann, D.H., Pashkovski, S.L., Guitchounts, G., Bozza, T., Datta, S.R., 2021. A transcriptional rheostat couples past activity to future sensory responses. Cell 184(26), 6326-6343 e6332. https://doi.org/10.1016/j.cell.2021.11.022.
Ualiyeva, S., Lemire, E., Wong, C., Perniss, A., Boyd, A.A., Aviles, E.C., Minichetti, D.G., Maxfield, A., Roditi, R., Matsumoto, I., Wang, X., Deng, W., Barrett, N.A., Buchheit, K.M., Laidlaw, T.M., Boyce, J.A., Bankova, L.G., Haber, A.L., 2024. A nasal cell atlas reveals heterogeneity of tuft cells and their role in directing olfactory stem cell proliferation. Sci Immunol 9(92), eabq4341. https://doi.org/10.1126/sciimmunol.abq4341.
Van Otterloo, E., Milanda, I., Pike, H., Thompson, J.A., Li, H., Jones, K.L., Williams, T., 2022. AP-2α and AP-2β cooperatively function in the craniofacial surface ectoderm to regulate chromatin and gene expression dynamics during facial development. Elife 11, e70511.
Wan, H., Dingle, S., Xu, Y., Besnard, V., Kaestner, K.H., Ang, S.L., Wert, S., Stahlman, M.T., Whitsett, J.A., 2005. Compensatory roles of Foxa1 and Foxa2 during lung morphogenesis. J Biol Chem 280(14), 13809-13816. https://doi.org/10.1074/jbc.M414122200.
Wolf, F.A., Angerer, P., Theis, F.J., 2018. SCANPY: large-scale single-cell gene expression data analysis. Genome Biol 19(1), 15. https://doi.org/10.1186/s13059-017-1382-0.
Wolf, F.A., Hamey, F.K., Plass, M., Solana, J., Dahlin, J.S., Gottgens, B., Rajewsky, N., Simon, L., Theis, F.J., 2019. PAGA: graph abstraction reconciles clustering with trajectory inference through a topology preserving map of single cells. Genome Biol 20(1), 59. https://doi.org/10.1186/s13059-019-1663-x.
Wolock, S.L., Lopez, R., Klein, A.M., 2019. Scrublet: Computational Identification of Cell Doublets in Single-Cell Transcriptomic Data. Cell Syst 8(4), 281-291 e289. https://doi.org/10.1016/j.cels.2018.11.005.
Yang, J., Shi, P., Li, Y., Zuo, Y., Nie, Y., Xu, T., Peng, D., An, Z., Huang, T., Zhang, J., Zhang, W., Xu, Y., Tang, Z., Li, A., Xu, J., 2024. Regulatory mechanisms orchestrating cellular diversity of Cd36+ olfactory sensory neurons revealed by scRNA-seq and scATAC-seq analysis. Cell Rep 43(9), 114671. https://doi.org/10.1016/j.celrep.2024.114671.
Yang, L.M., Huh, S.H., Ornitz, D.M., 2018. FGF20-Expressing, Wnt-Responsive Olfactory Epithelial Progenitors Regulate Underlying Turbinate Growth to Optimize Surface Area. Dev Cell 46(5), 564-580 e565. https://doi.org/10.1016/j.devcel.2018.07.010.
Ye, Q., Bhojwani, A., Hu, J.K., 2022. Understanding the development of oral epithelial organs through single cell transcriptomic analysis. Development 149(16), dev200539.
Yu, G., Wang, L.G., Han, Y., He, Q.Y., 2012. clusterProfiler: an R package for comparing biological themes among gene clusters. OMICS 16(5), 284-287. https://doi.org/10.1089/omi.2011.0118.

Yu, W., Sun, Z., Sweat, Y., Sweat, M., Venugopalan, S.R., Eliason, S., Cao, H., Paine, M.L., Amendt, B.A., 2020. Pitx2-Sox2-Lef1 interactions specify progenitor oral/dental epithelial cell signaling centers. Development 147(11), dev186023.

Yu, X., Ng, C.P., Habacher, H., Roy, S., 2008. Foxj1 transcription factors are master regulators of the motile ciliogenic program. Nature genetics 40(12), 1445-1453.

Zhu, X.J., Liu, Y., Yuan, X., Wang, M., Zhao, W., Yang, X., Zhang, X., Hsu, W., Qiu, M., Zhang, Z., Zhang, Z., 2016. Ectodermal Wnt controls nasal pit morphogenesis through modulation of the BMP/FGF/JNK signaling axis. Dev Dyn 245(3), 414-426. https://doi.org/10.1002/dvdy.24376.

Zwirner, S., Abu Rmilah, A.A., Klotz, S., Pfaffenroth, B., Kloevekorn, P., Moschopoulou, A.A., Schuette, S., Haag, M., Selig, R., Li, K., Zhou, W., Nelson, E., Poso, A., Chen, H., Amiot, B., Jia, Y., Minshew, A., Michalak, G., Cui, W., Rist, E., Longerich, T., Jung, B., Felgendreff, P., Trompak, O., Premsrirut, P.K., Gries, K., Muerdter, T.E., Heinkele, G., Wuestefeld, T., Shapiro, D., Weissbach, M., Koenigsrainer, A., Sipos, B., Ab, E., Zacarias, M.O., Theisgen, S., Gruenheit, N., Biskup, S., Schwab, M., Albrecht, W., Laufer, S., Nyberg, S., Zender, L., 2024. First-in-class MKK4 inhibitors enhance liver regeneration and prevent liver failure. Cell 187(7), 1666-1684 e1626. https://doi.org/10.1016/j.cell.2024.02.023.

FIGURE LEGEND

Fig. 1. Single-cell atlas of mouse embryonic nasal development.

A: Schematic overview of the scRNA-seq experimental design and analysis workflow for mouse nasal development from E10.5 to E18.5 (two biological replicates per time point). The resulting mouse nasal embryonic development cell atlas (mNEDCA) enables analysis of cell fate decisions, lineage trajectories, and intercellular communication.

B: UMAP visualization of 183,247 cells from mouse embryonic nasal tissue samples (n_pcs = 40, n_neighbors = 10). Each dot represents a cell. Left, colored by embryonic stage; Right, colored by annotated major cell type. UMAP, Uniform Manifold Approximation and Projection.

C: Dot plot showing expression of representative canonical markers for seven cell populations. Dot color indicates average expression level and dot size indicates the fraction of cells expressing each gene.

D: Pie chart representing the global proportions of the seven cell populations during the nasal development.

E: Stacked bar plot showing the fraction of seven cell populations across development stages (E10.5-E18.5). Colors correspond to panel (B).

F: Overview of the 52 distinct cell clusters of the mNEDCA, defined by hierarchical annotation and iterative sub-clustering.

Fig. 2. Molecular characterization of neurogenic and non-neurogenic nasal epithelial regions

A: UMAP visualization of 65,360 epithelial cells spanning neurogenic and non-neurogenic regions across developmental stages (n_pcs = 30, n_neighbors = 10). Each dot represents a cell.

B: UMAP visualization of the subdivision of neurogenic and non-neurogenic epithelium into distinct regions (respiratory, olfactory, vomeronasal, squamous, GnRH-1 neurons, terminal neurons and NC-derived cells). Cells are colored by annotated region identity.

C: Dot plot showing the expression of canonical markers and differentially expressed genes associated with different regions. Dot color indicates average expression level and dot size indicates the fraction of cells expressing each gene. Novel markers are highlighted in red.

D: Pie chart summarizing the global proportions of several regions across all stages. Colors correspond to panel (B).

E: Stacked bar plot illustrating the fraction of several regions across development stages. Colors correspond to panel (B).

F: SmFISH combined with immunofluorescence staining of E14.0 (top) and E18.0 (bottom) nasal tissue. Low-magnification scans (left) provide an overview of respiratory and olfactory regions. High-magnification views showing specific *Cyp4v3* (magenta) expression restricted to olfactory epithelium (middle; asterisks denote individual positive cells), and absent from respiratory epithelium (right). *Six3* (red) marks nasal epithelium and CDH1 (green)

immunofluorescence outlines epithelial boundaries. Images are representative of at least three independent experiments. Scale bars: 500 μm (left), 40 μm (middle/right); 10 μm for insets.

G: UMAP visualization of 1,615 ciliated cells from the respiratory epithelium (BBKNN integration, n_pcs = 30, n_neighbors = 50). Accompanying bar plot shows the number of cells contributed by each developmental stage.
H: UMAP feature plots showing the expression of *Foxj1* and *Sftpc* in the ciliated cells (color indicates normalized expression).
I: SmFISH combined with immunofluorescence staining of *Foxj1* and *Sftpc* in E18.0 nasal respiratory epithelium. High-magnification views showing *Foxj1*$^+$*Sftpc*$^+$ ciliated cells (arrowheads) and *Foxj1*$^+$*Sftpc*$^-$ ciliated cells (asterisk). CDH1 (green) immunofluorescence labels epithelial boundaries. Images are representative of at least three independent experiments. Scale bars: 50 μm; 20 μm for insets.

Fig. 3. Classification of nasal mesenchymal cells and key transcriptional regulation of MPCs

A: UMAP visualization of 105,140 nasal mesenchymal cells colored by different embryonic stages (Harmony integration, n_pcs = 30). Each dot represents a cell.
B: UMAP projection showing annotated major mesenchymal populations.
C: Dot plot showing the expression of marker genes across mesenchymal populations. Dot color indicates average expression level and dot size indicates the fraction of cells expressing each gene.
D: Pie chart representing the global proportions of major mesenchymal cell types. Colors correspond to panel (B).
E: Stacked bar plot illustrating the fraction of each major mesenchymal cell type across embryonic stages. Colors correspond to panel (B).
F: UMAP visualization of Mesenchymal stem cells (MSCs) and Mesenchymal progenitor cells (MPCs) colored by embryonic stages (BBKNN integration, n_pcs = 30). Each dot represents one cell.
G: Left, heatmap of genes shared or differentially expressed between MSCs and MPCs (Wilcoxon rank-sum test, $P < 0.01$), selected genes are labelled. Right, GO enrichment analysis of the identified DEGs, significance is indicated by *P*-values.
H: Heatmap of regulon activity (AUC scores) in MSCs versus MPCs inferred by pySCENIC. AUC scores were calculated at the single-cell level and averaged per cell type. Regulons are row-z-score normalized. TF families are annotated on the left. Regulons were filtered for measurable activity (see Methods).
I: UMAP feature plots showing the TF activity (blue, AUC score) and gene

expression (red, log-normalized) of MSCs-specific (*Hmga2*, *Alx3* and *Foxp1*), and MPCs-specific (*Nfix* and *Junb*). SCENIC-generated TF activity, represented by AUC score, reflects the co-expression strength of TF and its target genes.

Fig. 4. Niche homeostasis signaling in early respiratory epithelial progenitor cells

A: Circos plot of ligand-receptor (LR) interactions between non-/neurogenic epithelium and other major cell types across E10.5-E18.5. Ribbon widths represent the interaction weight. LR inference was performed with CellChat (see Methods). Epi., non-/neurogenic epithelium; Mesen., nasal mesenchyme; Glia, glia cells; Endo., endothelium; Imm., immune cells.

B: Dot plot showing the outgoing (secreted) and incoming (received) signals counts among major cell types. Dot size indicates population proportion.

C: Circos plot of LR interactions between RE progenitor cells and other cell types across E10.5-E11.5. Ribbon widths represent the interaction weight. RE pro., RE progenitor cells; OE, olfactory epithelium; MSCs, Mesenchymal stem cells; Endo., Endothelium; Imm., Immune cells.

D: Dot plot showing LR interaction strength related to panel (C). The color of each dot represents the communication probability. Only significant LR pairs are displayed (filtering criteria detailed in Methods).

E: Dot plot showing the expression of ligands in RE pro. across RE cell types (left) and developmental stages (right). BSCs, basal stem cells; BC, basal cells; SC, secretory cells; GC, goblet cells; GMC, glandular mucous cells; CC, ciliated cells.

F: Paired dot plots presenting the expression of ligands (left) and receptors (right) among RE pro. and interacting populations, color-coded by LR pairs. Dot color indicates average expression level and dot size indicates the fraction of cells expressing each gene.

G: Representative morphologies images of RE progenitor cells cultured after 7 days of induction in ALL and ALL-3C (without FGF8, DAPT and HRX215) medium. Images are representative of at least three independent experiments. Scale bars, 100 μm.

H: qRT–PCR quantification of progenitor marker (*Fgf8*, *Dlk1*) and differentiation marker (*Ltf* and *Cyp2f2*) after 7 days in ALL or ALL-3C medium. Data are mean ± SEM from $n = 3$ independent biological replicates. Statistical comparison was performed by ordinary one-way ANOVA followed by Dunnett's post-hoc test; significance thresholds are indicated in the panel (* $P < 0.05$; ** $P < 0.01$; *** $P < 0.001$ vs. the Primary RE progenitor cells).

I: Heatmap of RE progenitor-related and differentiation-related genes after 7 days in ALL or ALL-3C medium. Gene expression values were log-normalized for visualization.

J: Bar plot displays the GO terms enriched among genes that are upregulated

or downregulated in ALL-3C compared to ALL medium, with significance indicated by *P*-values.

K: Schematic model of in vitro maintenance of RE progenitor cells. Cells form compact spheroid in ALL medium but differentiate into cystic structures upon removal of FGF8, DAPT, and HRX215 (All-3C medium).

Fig. 5. Foxa1 as a key regulator of nasal respiratory epithelium differentiation

A: PHATE visualization of the respiratory epithelium colored by cell types (10,432 cells). RNA velocity vectors were projected onto the graph to infer directional lineage progression (see Methods). PHATE, Potential of Heat-diffusion for Affinity-based Trajectory Embedding.

B: PHATE embedding colored by embryonic stage, showing the temporal distribution of respiratory epithelial cells.

C: PHATE graph of respiratory epithelium colored by Diffusion Pseudotime (DPT). The gradient from dark purple to bright yellow represents the predicted differentiation progression.

D: Heatmap of genes differentially expressed along pseudotime trajectory; selected genes are labelled and TFs are highlighted in red (Wilcoxon rank-sum test, $P < 0.01$).

E: PHATE graph showing the TF activity (blue, AUC score) and gene expression (red, log-normalized) for RE differentiation-specific TFs (*Foxa1* and *Cebpd*), and RE progenitors-specific TFs (*Hmga2* and *Sp5*). TF activity was inferred using pySCENIC.

F: Transcriptional regulatory network centered on *Foxa1* nodes; edges denote regulatory links retained after cis-motif pruning (pySCENIC). Genes associated with ciliary function are highlighted in red.

G: Schematic of the in vitro overexpression experiment in primary RE progenitor cells. Cells were transduced with *Foxa1* overexpression (Foxa1) or DsRed (Ctrl), and cultured under defined induction conditions in ALL medium.

H: Heatmap showing the differential gene expression between Ctrl (DsRed) and Foxa1 overexpression conditions. Gene expression values (TPM values) were log-normalized for visualization.

I: Bar plot displaying the GO terms enriched among genes that are upregulated in *Foxa1* overexpression compared to Ctrl (DsRed), with enrichment significance indicated by *P*-values.

J: qRT-PCR quantification of Exo-*Foxa1*, *Foxj1* and *Sftpc* expression in Foxa1 overexpression versus Ctrl (DsRed). Data are mean ± SEM from n = 3 independent biological replicates. Statistical comparison was performed by two-tailed unpaired *t*-test; significance thresholds are indicated in the panel (* $P < 0.05$; ** $P < 0.01$ vs. the Ctrl).

Fig. 6. Differential characteristics of OPPs and GBCs and the heterogeneity during GBCs development

A: UMAP visualization of OPPs and GBCs (5,112 cells) colored by cell type (left) and embryonic stage (right) (n_pcs = 30, n_neighbors = 10). Each dot represents a cell.

B: Bar plot indicating the cell counts of OPPs and GBCs across developmental stages.

C: UMAP showing the expression of canonical marker genes *Sox2*, *Pax6*, *Ascl1* and *Kit* (log-normalized). *Sox2* and *Pax6* mark both OPPs and GBCs, while *Ascl1* and *Kit* are enriched in GBCs and low in OPPs.

D: Left, heatmap of genes shared or differentially expressed between OPPs and GBCs (Wilcoxon rank-sum test, $P < 0.01$), selected genes are labelled. Right, GO enrichment analysis of the identified DEGs, significance is indicated by *P*-values.

E: SmFISH and immunofluorescence staining of E11.5 (left) and E14.5 (right) nasal olfactory epithelium. High-magnification views showing specific *Sox2* (red) and *Car14* (magenta) expression restricted to OPPs (Left; asterisks denote individual positive cells), and specific *Ascl1* (red) and *Lgr5* (magenta) expression restricted to GBCs (right; asterisks denote individual positive cells). CDH1 (green) immunofluorescence outlines epithelial boundaries. Images are representative of at least three independent experiments. Scale bars, 40 μm; 10 μm for insets.

F: UMAP visualization of GBCs (2,714 cells) across different embryonic and postnatal stages (top) and subdivided into four subtypes (bottom) (n_pcs = 30, n_neighbors = 15). P19: Postnatal 19 day (Yang et al., 2024); P8W: Postnatal week 8 (Horgue et al., 2022); P11W-P36W: Postnatal week 11 to 36 (Ualiyeva et al., 2024).

G: Left, heatmap of differentially expressed genes among the four GBC subtypes (Wilcoxon rank-sum test, *P* value < 0.01), selected genes are labelled. Right, bar plot displays GO terms enriched among these genes, with enrichment significance indicated by *P*-values.

Figure 1

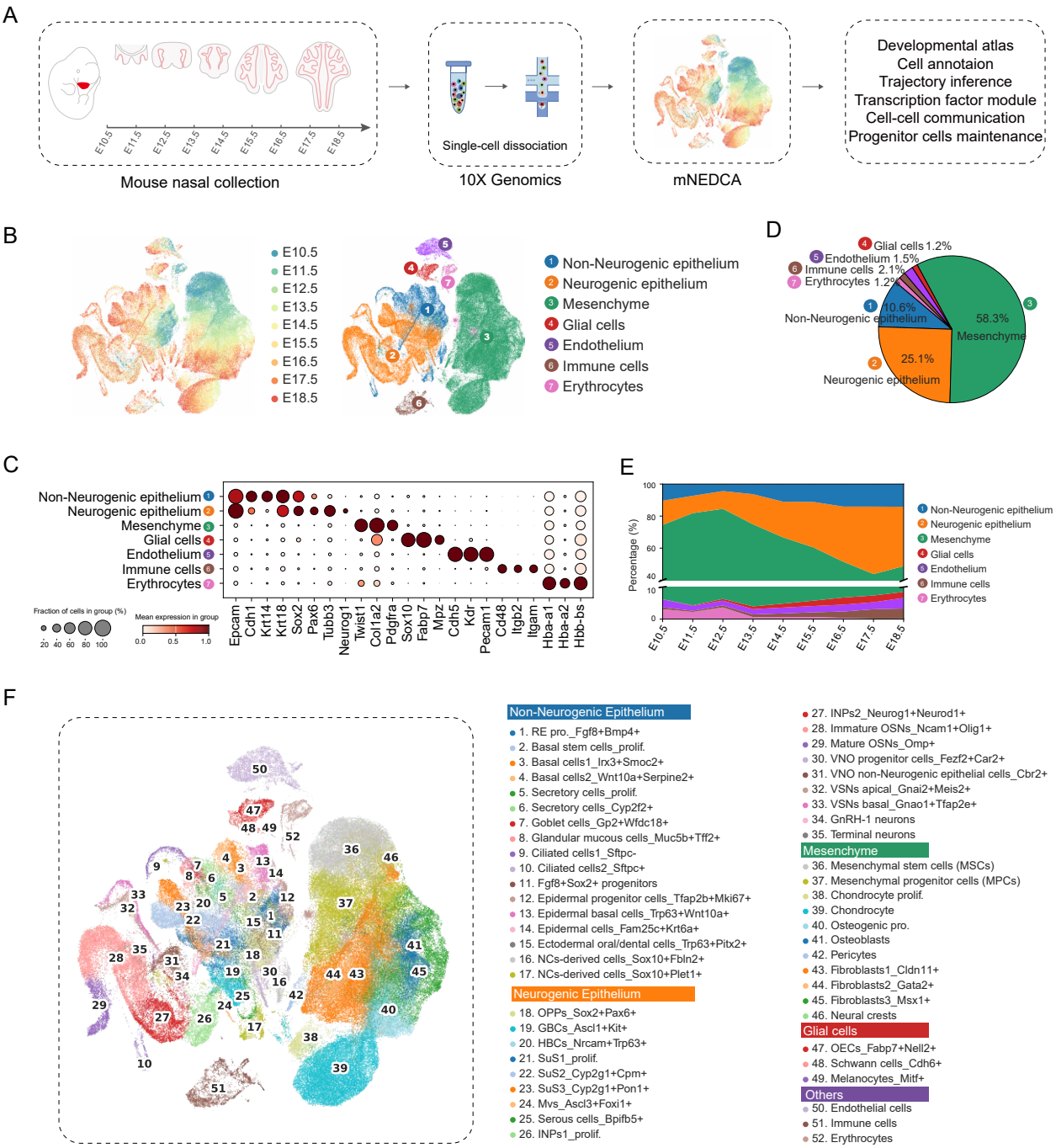
A
E10.5
E11.5
E12.5
E13.5
E14.5
E15.5
E16.5
E17.5
E18.5
Mouse nasal collection
Single-cell dissociation
10X Genomics
mNEDCA
Developmental atlas
Cell annotaion
Trajectory inference
Transcription factor module
Cell-cell communication
Progenitor cells maintenance
B
E10.5
E11.5
E12.5
E13.5
E14.5
E15.5
E16.5
E17.5
E18.5
Non-Neurogenic epithelium
Neurogenic epithelium
Mesenchyme
Glial cells
Endothelium
Immune cells
Erythrocytes
D
Glial cells 1.2%
Endothelium 1.5%
Immune cells 2.1%
Erythrocytes 1.2%
10.6%
Non-Neurogenic epithelium
58.3%
Mesenchyme
25.1%
Neurogenic epithelium
C
Non-Neurogenic epithelium
Neurogenic epithelium
Mesenchyme
Glial cells
Endothelium
Immune cells
Erythrocytes
Epcam
Cdh1
Krt14
Krt18
Sox2
Pax6
Tubb3
Neurog1
Twist1
Col1a2
Pdgfra
Sox10
Fabp7
Mpz
Cdh5
Kdr
Pecam1
Cd48
Itgb2
Itgam
Hba-a1
Hba-a2
Hbb-bs
Fraction of cells in group (%)
20 40 60 80 100
Mean expression in group
0.0 0.5 1.0
E
Percentage (%)
100
80
60
40
10
0
E10.5
E11.5
E12.5
E13.5
E14.5
E15.5
E16.5
E17.5
E18.5
Non-Neurogenic epithelium
Neurogenic epithelium
Mesenchyme
Glial cells
Endothelium
Immune cells
Erythrocytes
F
Non-Neurogenic Epithelium
1. RE pro._Fgf8+Bmp4+
2. Basal stem cells_prolif.
3. Basal cells1_Irx3+Smoc2+
4. Basal cells2_Wnt10a+Serpine2+
5. Secretory cells_prolif.
6. Secretory cells_Cyp2f2+
7. Goblet cells_Gp2+Wfdc18+
8. Glandular mucous cells_Muc5b+Tff2+
9. Ciliated cells1_Sftpc-
10. Ciliated cells2_Sftpc+
11. Fgf8+Sox2+ progenitors
12. Epidermal progenitor cells_Tfap2b+Mki67+
13. Epidermal basal cells_Trp63+Wnt10a+
14. Epidermal cells_Fam25c+Krt6a+
15. Ectodermal oral/dental cells_Trp63+Pitx2+
16. NCs-derived cells_Sox10+Fbln2+
17. NCs-derived cells_Sox10+Plet1+
Neurogenic Epithelium
18. OPPs_Sox2+Pax6+
19. GBCs_Ascl1+Kit+
20. HBCs_Nrcam+Trp63+
21. SuS1_prolif.
22. SuS2_Cyp2g1+Cpm+
23. SuS3_Cyp2g1+Pon1+
24. Mvs_Ascl3+Foxi1+
25. Serous cells_Bpifb5+
26. INPs1_prolif.
27. INPs2_Neurog1+Neurod1+
28. Immature OSNs_Ncam1+Olig1+
29. Mature OSNs_Omp+
30. VNO progenitor cells_Fezf2+Car2+
31. VNO non-Neurogenic epithelial cells_Cbr2+
32. VSNs apical_Gnai2+Meis2+
33. VSNs basal_Gnao1+Tfap2e+
34. GnRH-1 neurons
35. Terminal neurons
Mesenchyme
36. Mesenchymal stem cells (MSCs)
37. Mesenchymal progenitor cells (MPCs)
38. Chondrocyte prolif.
39. Chondrocyte
40. Osteogenic pro.
41. Osteoblasts
42. Pericytes
43. Fibroblasts1_Cldn11+
44. Fibroblasts2_Gata2+
45. Fibroblasts3_Msx1+
46. Neural crests
Glial cells
47. OECs_Fabp7+Nell2+
48. Schwann cells_Cdh6+
49. Melanocytes_Mitf+
Others
50. Endothelial cells
51. Immune cells
52. Erythrocytes

Figure 2

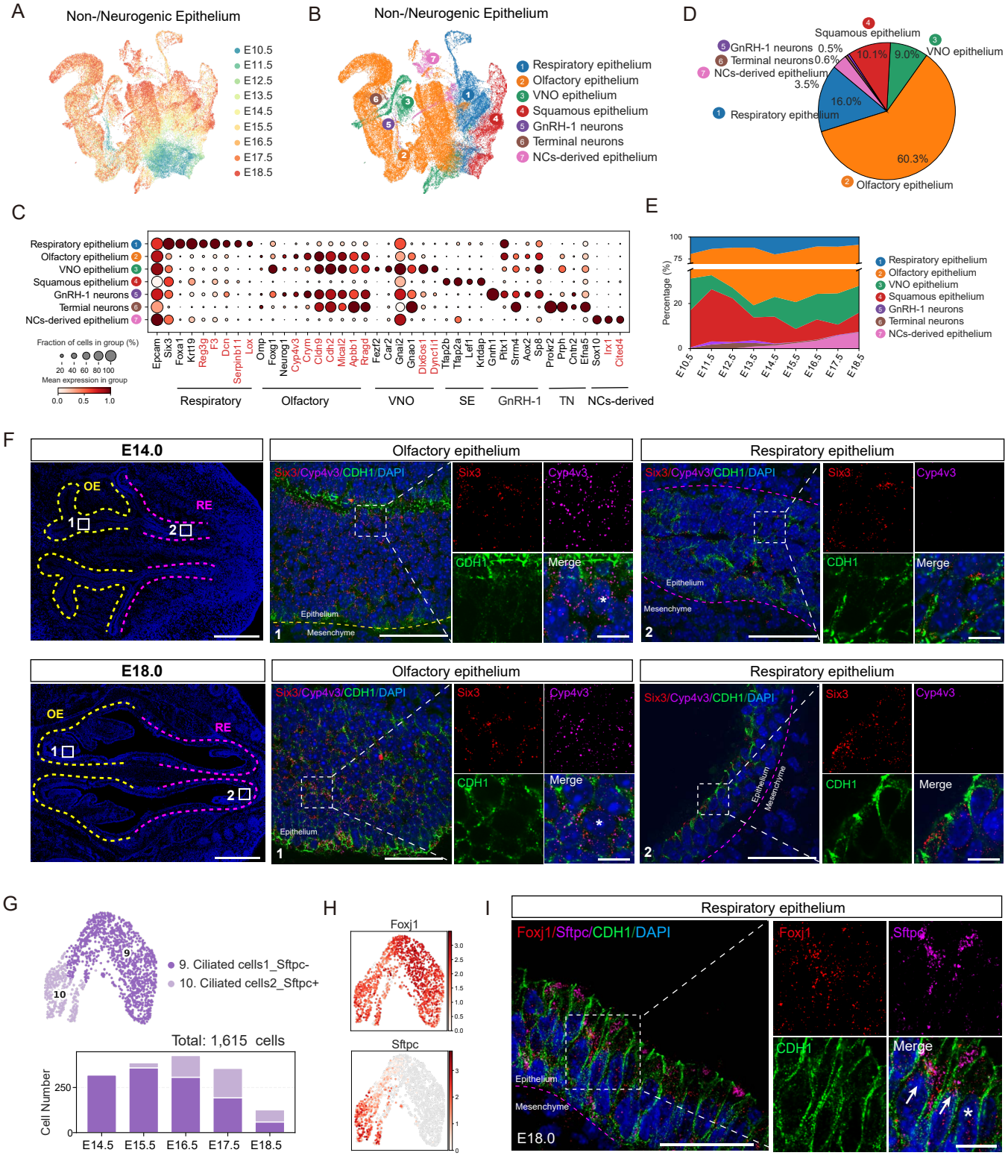
A
Non-/Neurogenic Epithelium
E10.5
E11.5
E12.5
E13.5
E14.5
E15.5
E16.5
E17.5
E18.5
B
Non-/Neurogenic Epithelium
1 Respiratory epithelium
2 Olfactory epithelium
3 VNO epithelium
4 Squamous epithelium
5 GnRH-1 neurons
6 Terminal neurons
7 NCs-derived epithelium
D
Squamous epithelium
VNO epithelium
GnRH-1 neurons 0.5%
Terminal neurons 0.6%
NCs-derived epithelium 3.5%
Respiratory epithelium
Olfactory epithelium
10.1%
9.0%
16.0%
60.3%
C
Respiratory epithelium
Olfactory epithelium
VNO epithelium
Squamous epithelium
GnRH-1 neurons
Termial neurons
NCs-derived epithelium
Epcam Six3 Foxa1 Krt19 Reg3g F3 Dcn Serpinb11 Lox Omp Foxg1 Neurog1 Cyp4v3 Crym Cldn9 Cdh2 Mical2 Apbb1 Rxgd Fezf2 Car2 Gnal2 Gnao1 Dlx6os1 Dync1i1 Tfap2b Tfap2a Lef1 Krtdap Gnrh1 Ptx1 Srrm4 Aox2 Sp8 Prokr2 Prph Chtr2 Elfa5 Sox10 Irx1 Cited4
Fraction of cells in group (%)
20 40 60 80 100
Mean expression in group
0.0 0.5 1.0
Respiratory
Olfactory
VNO
SE
GnRH-1
TN
NCs-derived
E
Percentage (%)
100
75
20
0
E10.5 E11.5 E12.5 E13.5 E14.5 E15.5 E16.5 E17.5 E18.5
F
E14.0
OE
RE
Olfactory epithelium
Respiratory epithelium
Six3/Cyp4v3/CDH1/DAPI
Six3
Cyp4v3
CDH1
Merge
Epithelium
Mesenchyme
E18.0
G
9. Ciliated cells1_Sftpc-
10. Ciliated cells2_Sftpc+
Total: 1,615 cells
Cell Number
250
0
E14.5 E15.5 E16.5 E17.5 E18.5
H
Foxj1
Sftpc
I
Respiratory epithelium
Foxj1/Sftpc/CDH1/DAPI
Foxj1
Sftpc
CDH1
Merge
Epithelium
Mesenchyme
E18.0

Figure 3

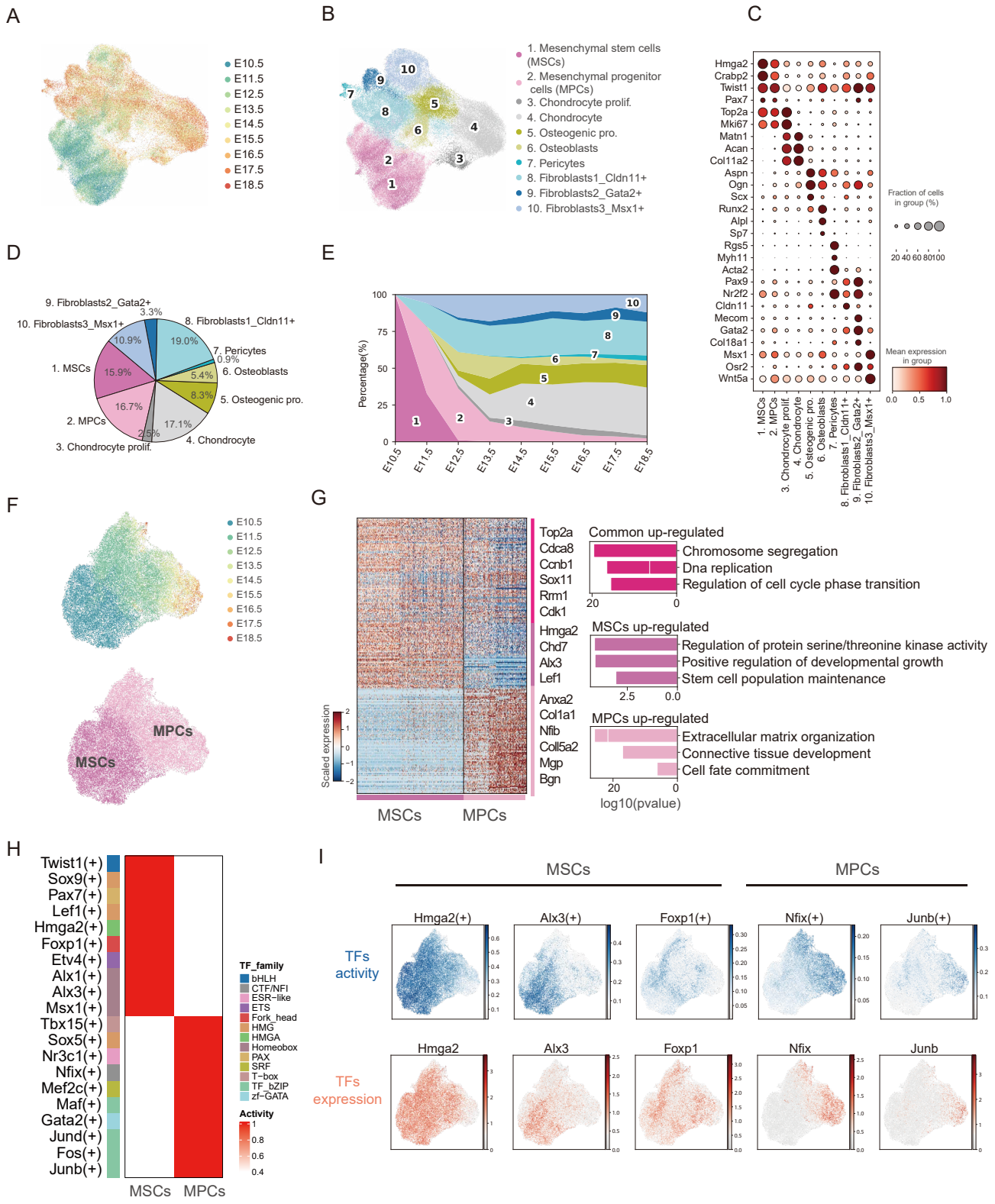
A
E10.5
E11.5
E12.5
E13.5
E14.5
E15.5
E16.5
E17.5
E18.5
B
1. Mesenchymal stem cells (MSCs)
2. Mesenchymal progenitor cells (MPCs)
3. Chondrocyte prolif.
4. Chondrocyte
5. Osteogenic pro.
6. Osteoblasts
7. Pericytes
8. Fibroblasts1_Cldn11+
9. Fibroblasts2_Gata2+
10. Fibroblasts3_Msx1+
C
Hmga2
Crabp2
Twist1
Pax7
Top2a
Mki67
Matn1
Acan
Col11a2
Aspn
Ogn
Scx
Runx2
Alpl
Sp7
Rgs5
Myh11
Acta2
Pax9
Nr2f2
Cldn11
Mecom
Gata2
Col18a1
Msx1
Osr2
Wnt5a
Fraction of cells in group (%)
20 40 60 80100
Mean expression in group
0.0 0.5 1.0
D
9. Fibroblasts2_Gata2+ 3.3%
10. Fibroblasts3_Msx1+ 10.9%
8. Fibroblasts1_Cldn11+ 19.0%
7. Pericytes 0.9%
1. MSCs 15.9%
6. Osteoblasts 5.4%
5. Osteogenic pro. 8.3%
2. MPCs 16.7%
4. Chondrocyte 17.1%
3. Chondrocyte prolif. 2.5%
E
Percentage(%)
E10.5 E11.5 E12.5 E13.5 E14.5 E15.5 E16.5 E17.5 E18.5
F
MPCs
MSCs
G
Scaled expression
MSCs MPCs
Top2a
Cdca8
Ccnb1
Sox11
Rrm1
Cdk1
Common up-regulated
Chromosome segregation
Dna replication
Regulation of cell cycle phase transition
Hmga2
Chd7
Alx3
Lef1
MSCs up-regulated
Regulation of protein serine/threonine kinase activity
Positive regulation of developmental growth
Stem cell population maintenance
Anxa2
Col1a1
Nfib
Col5a2
Mgp
Bgn
MPCs up-regulated
Extracellular matrix organization
Connective tissue development
Cell fate commitment
log10(pvalue)
H
Twist1(+)
Sox9(+)
Pax7(+)
Lef1(+)
Hmga2(+)
Foxp1(+)
Etv4(+)
Alx1(+)
Alx3(+)
Msx1(+)
Tbx15(+)
Sox5(+)
Nr3c1(+)
Nfix(+)
Mef2c(+)
Maf(+)
Gata2(+)
Jund(+)
Fos(+)
Junb(+)
MSCs MPCs
TF_family
bHLH
CTF/NFI
ESR-like
ETS
Fork_head
HMG
HMGA
Homeobox
PAX
SRF
T-box
TF_bZIP
zf-GATA
Activity
I
MSCs
MPCs
TFs activity
Hmga2(+)
Alx3(+)
Foxp1(+)
Nfix(+)
Junb(+)
TFs expression
Hmga2
Alx3
Foxp1
Nfix
Junb

Figure 4

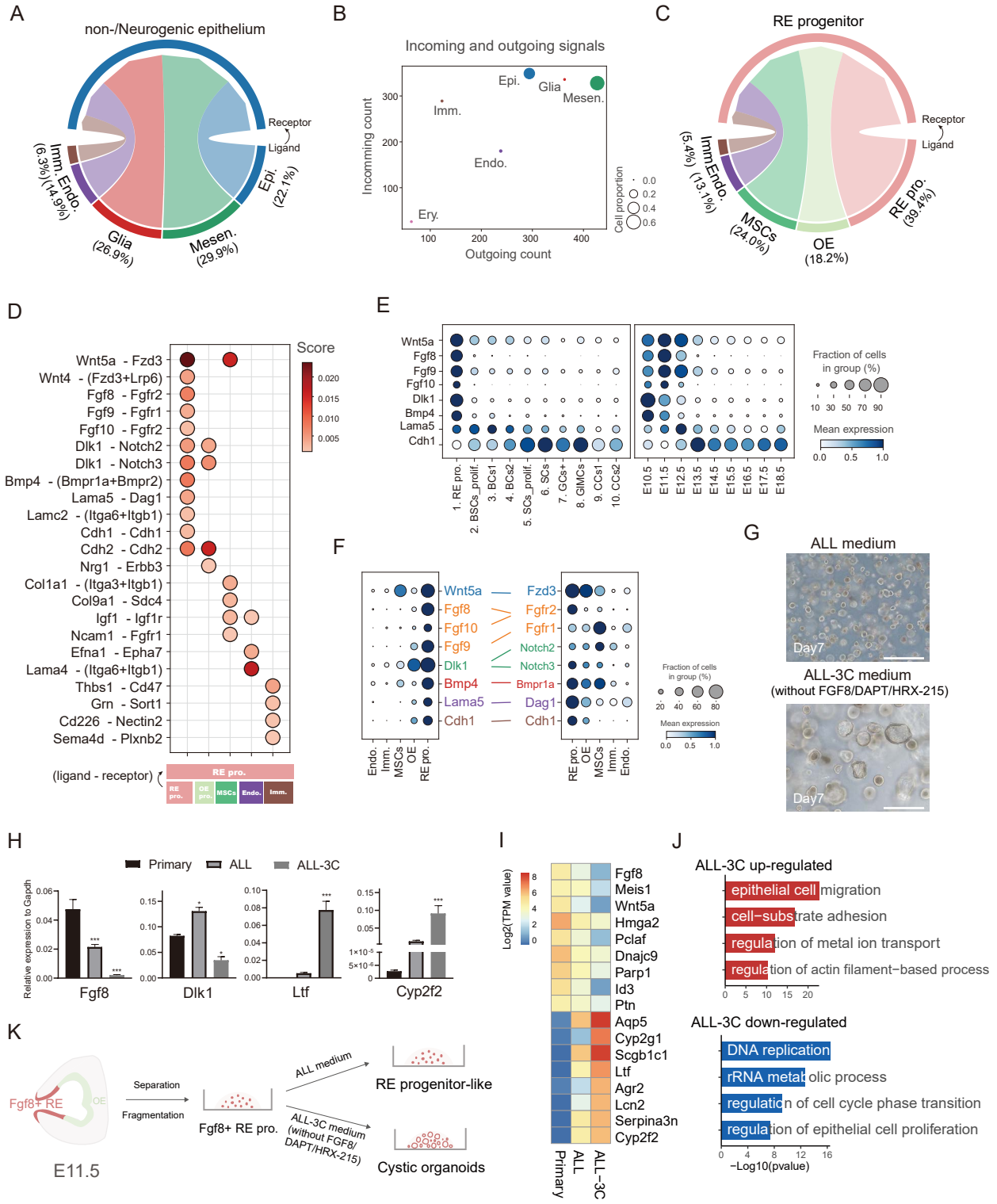
A
non-/Neurogenic epithelium
Receptor
Ligand
Epi. (22.1%)
Mesen. (29.9%)
Glia (26.9%)
Imm. (6.3%)
Endo. (14.9%)
B
Incoming and outgoing signals
Incomming count
Outgoing count
Epi.
Glia
Mesen.
Imm.
Endo.
Ery.
Cell proportion
C
RE progenitor
Receptor
Ligand
RE pro. (39.4%)
OE (18.2%)
MSCs (24.0%)
Endo. (13.1%)
Imm. (5.4%)
D
Score
Wnt5a - Fzd3
Wnt4 - (Fzd3+Lrp6)
Fgf8 - Fgfr2
Fgf9 - Fgfr1
Fgf10 - Fgfr2
Dlk1 - Notch2
Dlk1 - Notch3
Bmp4 - (Bmpr1a+Bmpr2)
Lama5 - Dag1
Lamc2 - (Itga6+Itgb1)
Cdh1 - Cdh1
Cdh2 - Cdh2
Nrg1 - Erbb3
Col1a1 - (Itga3+Itgb1)
Col9a1 - Sdc4
Igf1 - Igf1r
Ncam1 - Fgfr1
Efna1 - Epha7
Lama4 - (Itga6+Itgb1)
Thbs1 - Cd47
Grn - Sort1
Cd226 - Nectin2
Sema4d - Plxnb2
(ligand - receptor)
RE pro.
E
Fraction of cells in group (%)
Mean expression
1. RE pro.
2. BSCs_prolif.
3. BCs1
4. BCs2
5. SCs_prolif.
6. SCs
7. GCs+
8. GIMCs
9. CCs1
10. CCs2
E10.5
E11.5
E12.5
E13.5
E14.5
E15.5
E16.5
E17.5
E18.5
F
Wnt5a
Fgf8
Fgf10
Fgf9
Dlk1
Bmp4
Lama5
Cdh1
Fzd3
Fgfr2
Fgfr1
Notch2
Notch3
Bmpr1a
Dag1
Cdh1
G
ALL medium
Day7
ALL-3C medium
(without FGF8/DAPT/HRX-215)
Day7
H
Primary
ALL
ALL-3C
Relative expression to Gapdh
Fgf8
Dlk1
Ltf
Cyp2f2
I
Log2(TPM value)
Fgf8
Meis1
Wnt5a
Hmga2
Pclaf
Dnajc9
Parp1
Id3
Ptn
Aqp5
Cyp2g1
Scgb1c1
Ltf
Agr2
Lcn2
Serpina3n
Cyp2f2
Primary
ALL
ALL-3C
J
ALL-3C up-regulated
epithelial cell migration
cell-substrate adhesion
regulation of metal ion transport
regulation of actin filament-based process
ALL-3C down-regulated
DNA replication
rRNA metabolic process
regulation of cell cycle phase transition
regulation of epithelial cell proliferation
-Log10(pvalue)
K
Fgf8+ RE
OE
E11.5
Separation
Fragmentation
Fgf8+ RE pro.
ALL medium
RE progenitor-like
ALL-3C medium (without FGF8/DAPT/HRX-215)
Cystic organoids

Figure 5

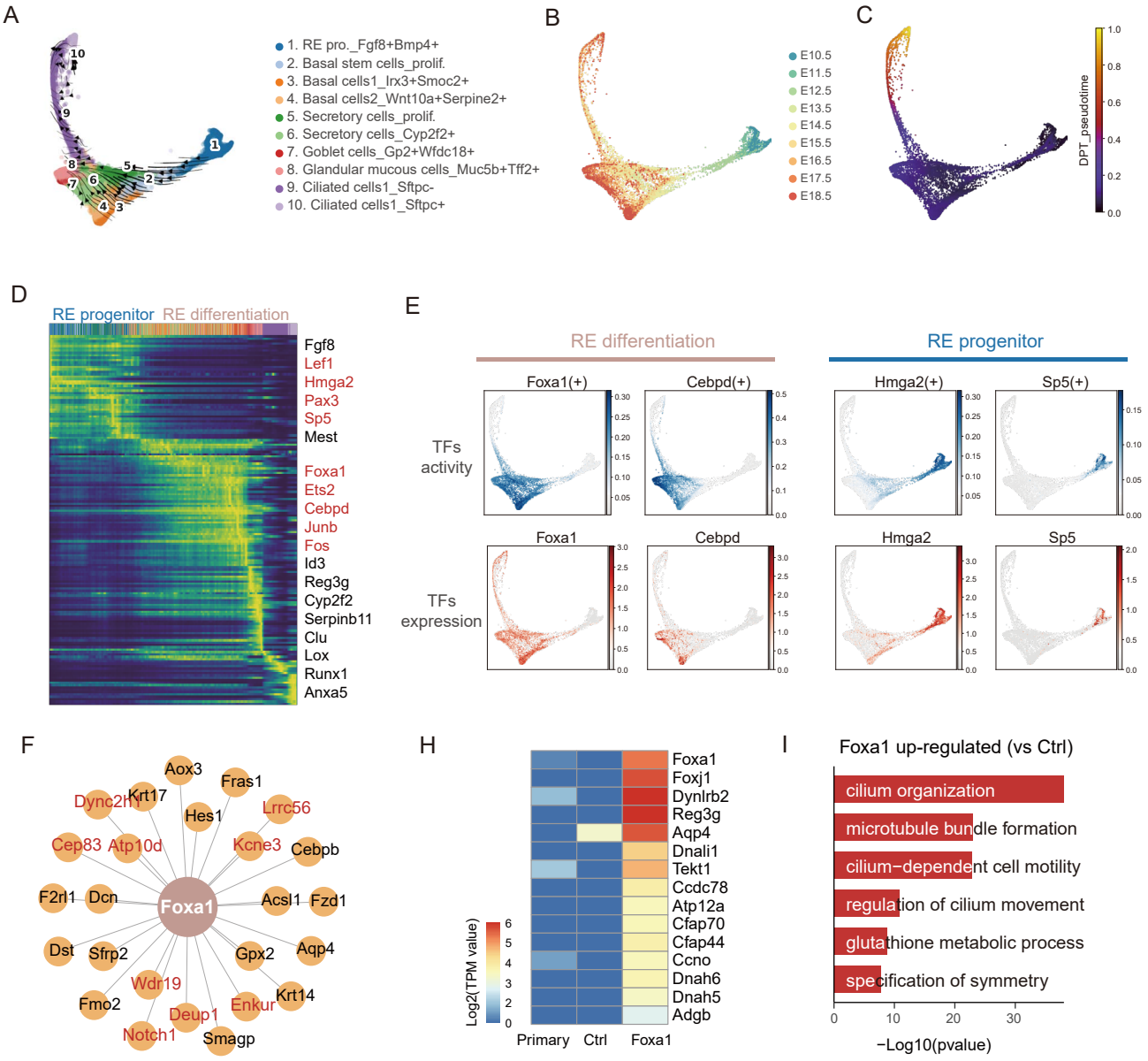
A
1. RE pro._Fgf8+Bmp4+
2. Basal stem cells_prolif.
3. Basal cells1_Irx3+Smoc2+
4. Basal cells2_Wnt10a+Serpine2+
5. Secretory cells_prolif.
6. Secretory cells_Cyp2f2+
7. Goblet cells_Gp2+Wfdc18+
8. Glandular mucous cells_Muc5b+Tff2+
9. Ciliated cells1_Sftpc-
10. Ciliated cells1_Sftpc+
B
E10.5
E11.5
E12.5
E13.5
E14.5
E15.5
E16.5
E17.5
E18.5
C
DPT_pseudotime
D
RE progenitor
RE differentiation
Fgf8
Lef1
Hmga2
Pax3
Sp5
Mest
Foxa1
Ets2
Cebpd
Junb
Fos
Id3
Reg3g
Cyp2f2
Serpinb11
Clu
Lox
Runx1
Anxa5
E
RE differentiation
RE progenitor
TFs activity
TFs expression
Foxa1(+)
Cebpd(+)
Hmga2(+)
Sp5(+)
Foxa1
Cebpd
Hmga2
Sp5
F
Foxa1
Aox3
Fras1
Dync2h1
Krt17
Hes1
Lrrc56
Cep83
Atp10d
Kcne3
Cebpb
F2rl1
Dcn
Acsl1
Fzd1
Dst
Sfrp2
Gpx2
Aqp4
Wdr19
Fmo2
Deup1
Enkur
Krt14
Notch1
Smagp
H
Log2(TPM value)
Foxa1
Foxj1
Dynlrb2
Reg3g
Aqp4
Dnali1
Tekt1
Ccdc78
Atp12a
Cfap70
Cfap44
Ccno
Dnah6
Dnah5
Adgb
Primary
Ctrl
Foxa1
I
Foxa1 up-regulated (vs Ctrl)
cilium organization
microtubule bundle formation
cilium−dependent cell motility
regulation of cilium movement
glutathione metabolic process
specification of symmetry
−Log10(pvalue)
G
Primary RE pro.
Retrovirus carried DsRed/Foxa1
J
Exo-Foxa1
Foxj1
Dyn1rb2
Reg3g
Relative expression to Gapdh
Ctrl
Foxa1

Figure 6

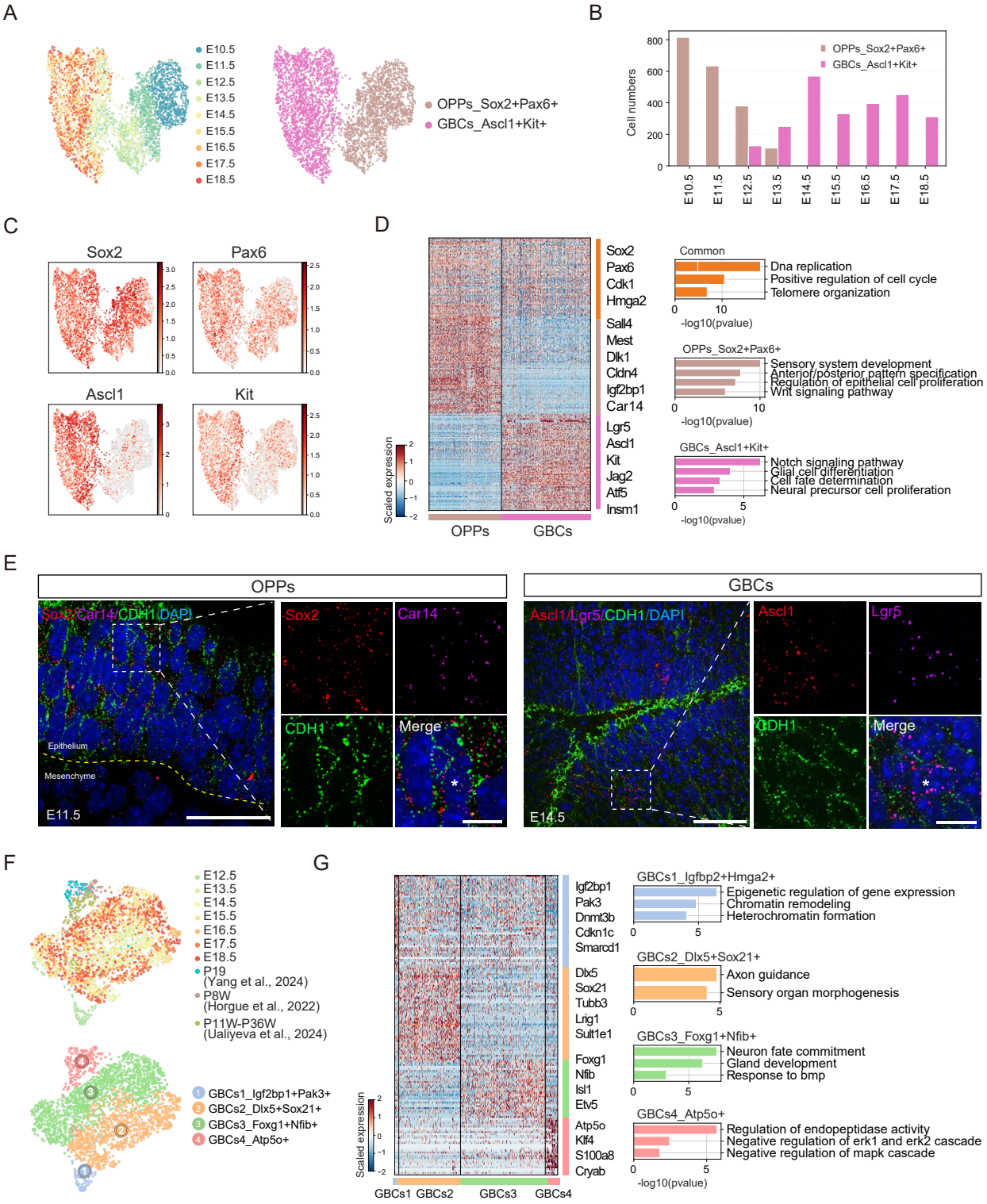
A
E10.5
E11.5
E12.5
E13.5
E14.5
E15.5
E16.5
E17.5
E18.5
OPPs_Sox2+Pax6+
GBCs_Ascl1+Kit+
B
Cell numbers
OPPs_Sox2+Pax6+
GBCs_Ascl1+Kit+
C
Sox2
Pax6
Ascl1
Kit
D
Scaled expression
OPPs
GBCs
Sox2
Pax6
Cdk1
Hmga2
Sall4
Mest
Dlk1
Cldn4
Igf2bp1
Car14
Lgr5
Ascl1
Kit
Jag2
Atf5
Insm1
Common
Dna replication
Positive regulation of cell cycle
Telomere organization
-log10(pvalue)
OPPs_Sox2+Pax6+
Sensory system development
Anterior/posterior pattern specification
Regulation of epithelial cell proliferation
Wnt signaling pathway
GBCs_Ascl1+Kit+
Notch signaling pathway
Glial cell differentiation
Cell fate determination
Neural precursor cell proliferation
E
OPPs
GBCs
Sox2/Car14/CDH1/DAPI
Sox2
Car14
CDH1
Merge
Epithelium
Mesenchyme
E11.5
Ascl1/Lgr5/CDH1/DAPI
Ascl1
Lgr5
CDH1
Merge
E14.5
F
E12.5
E13.5
E14.5
E15.5
E16.5
E17.5
E18.5
P19
(Yang et al., 2024)
P8W
(Horgue et al., 2022)
P11W-P36W
(Ualiyeva et al., 2024)
GBCs1_Igf2bp1+Pak3+
GBCs2_Dlx5+Sox21+
GBCs3_Foxg1+Nfib+
GBCs4_Atp5o+
G
Scaled expression
GBCs1
GBCs2
GBCs3
GBCs4
Igf2bp1
Pak3
Dnmt3b
Cdkn1c
Smarcd1
Dlx5
Sox21
Tubb3
Lrig1
Sult1e1
Foxg1
Nfib
Isl1
Etv5
Atp5o
Klf4
S100a8
Cryab
GBCs1_Igfbp2+Hmga2+
Epigenetic regulation of gene expression
Chromatin remodeling
Heterochromatin formation
GBCs2_Dlx5+Sox21+
Axon guidance
Sensory organ morphogenesis
GBCs3_Foxg1+Nfib+
Neuron fate commitment
Gland development
Response to bmp
GBCs4_Atp5o+
Regulation of endopeptidase activity
Negative regulation of erk1 and erk2 cascade
Negative regulation of mapk cascade
-log10(pvalue)